arXiv:2604.11331v2 [cs.CV] 19 Oct 2026

Any 3D Scene is Worth 1K Tokens: 3D-Grounded Representation for Scene Generation at Scale

Dongxu Wei[1,2,*] **Qi Xu**[1,*] **Zhiqi Li**[1,3] **Hangning Zhou**[2,†] **Cong Qiu**[2]
Hailong Qin[2] **Mu Yang**[2] **Zhaopeng Cui**[3] **Peidong Liu**[1✉]
[1]Westlake University [2]Afari Intelligent Drive [3]Zhejiang University
[*]Equal contribution. [†]Project Lead. [✉]Corresponding Author.
Project Page: wswdx.github.io/3DRAE

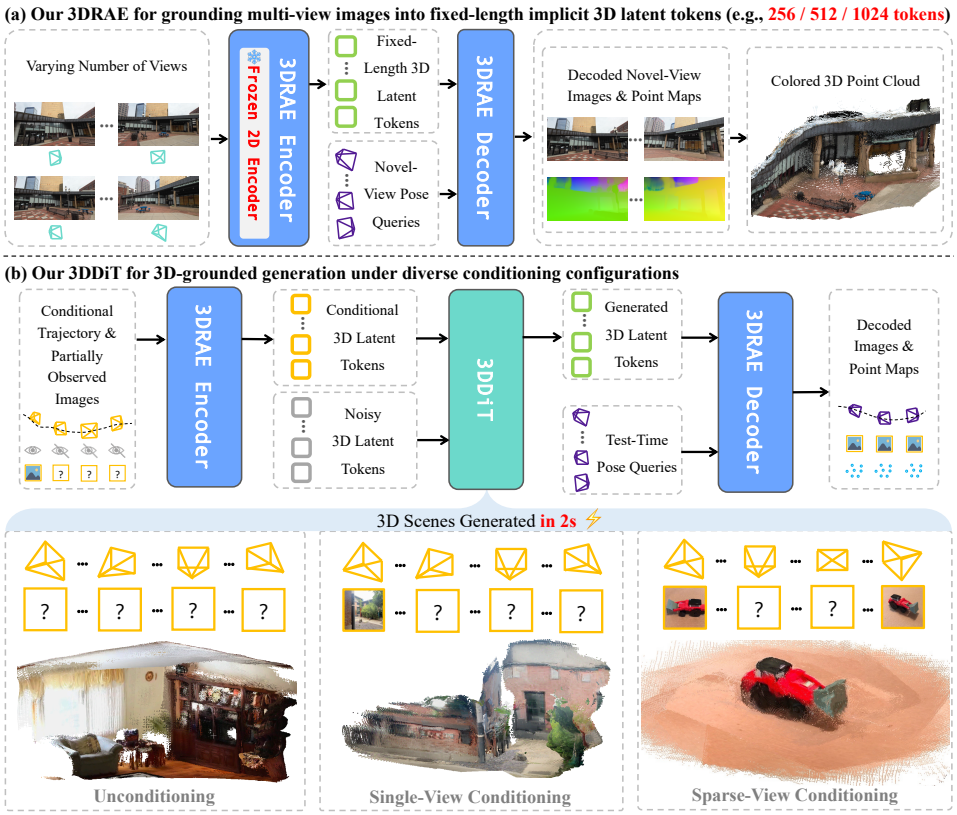


Figure 1: **3D-Grounded Scene Generation.** (a) Our 3DRAE repurposes frozen 2D foundation models to ground varying number of views into fixed-length implicit 3D latent tokens, which can be queried to decode images and point maps of various views including novel views. (b) Our 3DDiT performs diffusion modeling directly in this implicit 3D latent space, enabling 3D-grounded generation with superior efficiency and spatial consistency.

Abstract

Scene-level 3D generation has long been dominated by 2D multi-view or video diffusion models. Typically, these 2D-based approaches perform scene generation in a 2D latent space, which introduces two fundamental issues: (i) representing 3D scenes via 2D views leads to significant representation redundancy, and (ii) latent space rooted in 2D inherently limits the spatial consistency of the generated scenes. In this paper, we propose to perform 3D scene generation directly within a high-

40th Conference on Neural Information Processing Systems (NeurIPS 2026).

dimensional implicit 3D latent space derived from powerful 2D foundation models (e.g., DINOv2, SigLIP2, DA3). Then we tame diffusion transformers to perform diffusion modeling directly in the 3D latent space, enabling 3D-grounded scene generation. In our experiments, we not only demonstrate the advantages of our method over 2D-based approaches in terms of efficiency and spatial consistency, but also comprehensively analyze the impact of 3D latent representation on 3D scene generation performance. Furthermore, we validate the favorable scalability of our method with respect to representation and model capacity.

1 Introduction

If we paraphrase the recent literature by characterizing "the evolution of generative modeling as a continual redefinition of where and how models learn to represent data" [1], then in the domain of 3D generation, this exploration specifically focuses on how models learn to represent 3D data. Early methodologies attempted to leverage 3D priors such as triplanes [2–4], voxels [5–8] or neural radiance field [9–11] for 3D representation. Recently, with the advancement of video diffusion models [12–18], it is observed that these models can synthesize high-quality video sequences. This led to a paradigm shift: treating spatial extrapolation as a special case of temporal extension. By adapting video diffusion models—which inherently possess a prior for 2D temporal coherence—to the task of spatially-consistent multi-view image synthesis, these approaches achieve coherent generation of multi-view images that follow a long camera trajectory. This capability enables the simulation of navigation through 3D environments, and has thus become the prevailing approach in most contemporary 3D scene generation frameworks [19–30].



Figure 2: We empirically find that overlapping regions across multiple views correspond to the same set of tokens. Therefore, we employ fixed-length 3D latent tokens to eliminate such multi-view redundancy.

In essence, however, these methods remain rooted in 2D latent space rather than constituting truly 3D-grounded generation. The degradation of a 3D scene into 2D views introduces two fundamental issues: (1) *Representation Redundancy*: Significant cross-view overlap inherent in multi-view representations leads to substantial information redundancy. For instance, with a patch size of 16, depicting a 3D scene using 32 images at 256×256 resolution requires $32 \times 16 \times 16 = 8192$ tokens, whereas the actual number of unique informative tokens may be as low as 1024 due to cross-view overlap (Fig.2), incurring considerable computational waste. (2) *Limited Spatial Consistency*: As 2D diffusion models lack intrinsic 3D spatial modeling, the 3D scenes they generate through temporal extension inevitably suffer from spatial inconsistencies, where errors may accumulate as pose changes and finally lead to structural deterioration. Consequently, we pose a critical question: Given only data access to multi-view images or videos (as in previous 2D-based approaches), *is it possible to develop models that learn to transform 2D images into a 3D latent space? And can we perform diffusion modeling directly within the 3D latent space for 3D scene generation?* We conjecture that such 3D-grounded generation may not need to sacrifice efficiency or spatial consistency.

Motivated by this, our foremost task is to define a 3D latent space that can be derived from 2D images and grounded with 3D knowledge. One approach is to borrow from feed-forward 3D reconstruction methods, where novel view rendering [31–39] or point reconstruction [40–43] serves as supervision, enabling the model to recover 3D information from 2D images. However, most of these methods rely on pixel-aligned representations coupled with 2D views, which inevitably leads to representation redundancy. Very few approaches [44–46] attempt to map 2D images into a fixed-size set of implicit tokens, achieving decoupling from 2D views while remaining grounded in 3D. However, directly leveraging these high-dimensional tokens (e.g., 768-dim) to construct a latent space amenable to diffusion modeling is challenging and non-trivial, as diffusion models are generally known to struggle with denoising in high-dimensional spaces. Inspired by recent advances in representation autoencoders (RAE) [1, 47] that achieve single image diffusion directly in high-dimensional spaces

with rich semantics, we propose 3DRAE — a method that repurposes pre-trained 2D foundation models (e.g., DINOv2 [48], SigLIP2 [49], DA3 [43]) to encode varying number of 2D views into fixed-length implicit and 3D-grounded latent tokens (Fig.1-a). Then we introduce 3DDiT — a 3D-grounded diffusion transformer that performs 3D scene generation directly in the 3D latent space learned by our 3DRAE (Fig.1-b), enabling 3D-grounded generation with significantly improved efficiency and spatial consistency compared to prior 2D diffusion-based methods. Furthermore, we thoroughly investigated how 3D latent representations derived from different 2D foundation models impact 3D scene generation, and achieved a trade-off between reconstruction and generation capabilities across various design choices.

In summary, our main contributions are as follows:

- To our knowledge, this is the first work to extend single-image RAE to the 3D domain and thoroughly discuss the impact of 3D latent representation on 3D scene generation.
- Extensive experiments demonstrate the significant potential of our method over 2D diffusion-based methods, particularly in terms of efficiency and spatial consistency.
- Our method exhibits strong scalability in terms of both representation and model capacity, and we provide models of varying complexity to benefit the community.

2 Related Work

Scene-Level 3D Generation. With the advancement of open-source video diffusion models [13, 15, 16, 18], many 3D generation methods [19–30, 50] have emerged that incorporate camera conditions to synthesize videos following specified trajectories. These approaches effectively degrade 3D spatial extrapolation to 2D temporal extension. To improve spatial consistency, some methods [20, 21, 23] additionally predict 3DGS primitives alongside RGB during decoding, enabling 3D-aware synthesis. Others [28–30] maintain explicit 3D memory based on historical frames, and condition subsequent generation on historical renderings to enforce coherence. Despite these efforts, all such methods fundamentally operate in a 2D latent space, which introduces substantial representation redundancy and struggles to ensure spatial consistency at the 3D level. Another line of work [51, 52] focuses on object-level 3D generation. Leveraging massive high-quality 3D asset data, these methods achieve 3D generation in explicit 3D latent space based on point clouds or voxels. However, for scene-level generation, such high-quality 3D data is unavailable. How to achieve 3D-grounded scene generation using only multi-view image data remains a challenge.

Representation for 2D Diffusion. Recent work in 2D diffusion reveals that aligning the latent space with pre-trained representation encoders substantially improves 2D generation performance. Some approaches [53–56] align VAE latents with pretrained encoders or incorporate MAE [57] objectives into VAE training, significantly enhancing reconstruction quality. Others align intermediate diffusion features with pretrained encoders [58–60] or generate the features directly within a diffusion model [1, 47, 61], accelerating convergence. Among these, Representation Autoencoder (RAE) [1, 47] pioneers the use of frozen 2D foundation models as autoencoders for diffusion and generates high-dimensional latent tokens with rich semantics directly. This not only improves training stability and generation fidelity but also enables visual understanding and generation to operate within a shared representation, opening new possibilities for unified vision models. Inspired by RAE, we propose 3DRAE, which lifts 2D representations into a 3D latent space for 3D-grounded generation with superior efficiency and spatial consistency.

3 Method

3.1 Preliminaries

Autoencoders for Diffusion. Diffusion models operate through an encode-decode paradigm that maps data to a latent space and subsequently learn to generate samples within this latent space. Prior image or video diffusion approaches [12, 13, 15, 16, 18] typically employ channel-wise compressed VAE encoder $\mathcal{E}$ to map images into the 2D latent space, and use decoder $\mathcal{D}$ to reconstruct images from latents. For an image $I \in \mathbb{R}^{H\times W\times 3}$, the VAE pipeline follows:

$$I \xrightarrow{\mathcal{E}} z \xrightarrow{\mathcal{D}} \hat{I}, \quad \text{where } z = \mathcal{E}(I) \in \mathbb{R}^{h\times w\times c}, \tag{1}$$

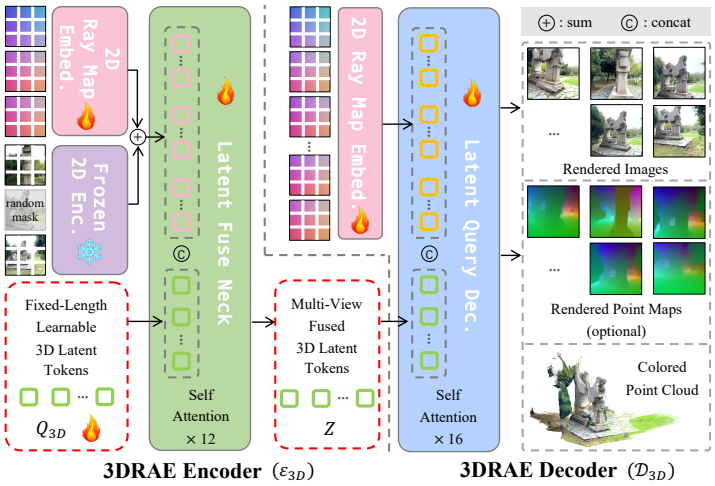


Figure 3: **The Architecture of Our 3DRAE.**

with spatial compression factor f such that $h = H/f, w = W/f$, and channel dimension c (e.g., $c = 4$). While efficient, such VAEs yield low-capacity latent optimized primarily for reconstruction, lacking the global semantic structure essential for robust generalization and generative performance.

A recent line of work [1, 47] introduces representation autoencoders (RAEs) to reformulate this pipeline using frozen visual encoders f_{enc} (e.g., DINOv2 [48], SigLIP2 [49]), which are primarily pretrained for semantic understanding. For an image I, the RAE mapping becomes:

$$I \xrightarrow{f_{\text{enc}}} z \xrightarrow{\mathcal{D}} \hat{I}, \quad \text{where } z = f_{\text{enc}}(I) \in \mathbb{R}^{n \times d}, \tag{2}$$

with patch size p such that the number of patch tokens $n = \frac{H}{p} \times \frac{W}{p}$, and feature dimension d (e.g., $d = 768$). Unlike VAEs, RAEs retain rich semantics without channel compression, significantly accelerating convergence of diffusion training and improving image fidelity. However, since the latent space of RAEs remains grounded at 2D image level, they cannot be used to represent 3D scenes.

3.2 3DRAE: 3D-Grounded Latent Representation Autoencoder

In this work, we demonstrate how to leverage pre-trained 2D foundation models to extract multi-view features, which are subsequently transformed into a 3D-grounded latent space endowed with rich 2D semantic information. Our approach encodes multi-view observations of a 3D scene into a compact representation consisting of fixed-length 3D latent tokens, from which various viewpoints including novel ones can be decoded, effectively decoupling 3D scene representation from input view observations.

3D Scene Encoding and Decoding. Given a set of N_{obs} observed multi-view images $\mathcal{I}_{\text{obs}} = \{I_i\}_{i=1}^{N_{\text{obs}}}$ with corresponding camera poses $\mathcal{P}_{\text{obs}} = \{P_i\}_{i=1}^{N_{\text{obs}}}$, our 3DRAE encoder $\mathcal{E}_{\text{3D}}$ establishes the mapping:

$$(\mathcal{I}_{\text{obs}}, \mathcal{P}_{\text{obs}}) \xrightarrow{\mathcal{E}_{\text{3D}}} Z, \quad \text{where } Z = \mathcal{E}_{\text{3D}}(\mathcal{I}_{\text{obs}}, \mathcal{P}_{\text{obs}}) \in \mathbb{R}^{m \times d}. \tag{3}$$

Here Z denotes 3D latent tokens of fixed length m, which compactly encodes the scene appearance and geometry. Notably, N_{obs} can vary to accommodate representation of 3D scenes observed by varying number of views.

As for decoding, our 3DRAE decoder $\mathcal{D}_{\text{3D}}$ is designed to recover appearance and geometry for varying views given the encoded 3D latent tokens Z. For example, for a camera trajectory $\mathcal{P}_{\text{dec}} = \{P_j\}_{j=1}^{N_{\text{dec}}}$ consisting of N_{dec} views to be decoded, the view-conditioned decoding then follows:

$$(Z, \mathcal{P}_{\text{dec}}) \xrightarrow{\mathcal{D}_{\text{3D}}} \{\hat{I}_j\}_{j=1}^{N_{\text{dec}}}, \quad \text{where } \hat{I}_j = \mathcal{D}_{\text{3D}}(Z, \psi(P_j)) \in \mathbb{R}^{H \times W \times 3}. \tag{4}$$

Here $\psi(P_j)$ generates ray map tokens that query Z to retrieve appearance and geometry for the specified view pose P_j. This formulation treats the 3D latent Z as a sufficient scene statistic: once encoded from partial observations, it enables rendering of the full scene given any camera pose along the trajectory $\mathcal{P}_{\text{obs}}$, effectively transforming partial observations into a complete 3D representation.

Model Design. As illustrated in Fig.3, our 3DRAE encoder $\mathcal{E}_{\text{3D}}$ incorporates a frozen 2D image encoder f_{enc} and a 2D ray map embedding module ψ to extract multi-view visual and geometric

information, respectively. Their outputs are summed to form a dense set of multi-view patch tokens:

$$t_i = f_{\text{enc}}(I_i) + \psi(P_i) \in \mathbb{R}^{n \times d}, \quad \text{for } i = 1, \ldots, N_{\text{obs}}. \tag{5}$$

Subsequently, we introduce a Latent Fuse Neck, which concatenates a fixed-length set of learnable 3D latent tokens $Q_Z \in \mathbb{R}^{m \times d}$ with the multi-view patch tokens $\{t_i\}_{i=1}^{N_{\text{obs}}}$. The combined tokens are processed through a 12-layer transformer with self attention, enabling deep cross-modal information fusion. The output is a set of multi-view fused 3D latent tokens $Z \in \mathbb{R}^{m \times d}$ that encapsulate comprehensive 3D scene information after spatial redundancy reduction.

Next, we employ a latent query decoder $\mathcal{D}_{\text{3D}}$ consisting of a 16-layer transformer with self attention to integrate ray map tokens $\psi(P_j)$ of target views with the encoded 3D latent tokens Z, where the ray map tokens query and retrieve relevant information for synthesizing the target views. The resulting ray map tokens from the final decoder layer are then unpatchified to image renderings. Meanwhile, another latent query decoder with DPT head [62] is optionally employed to produce 3D point maps for the target views, where the DPT head processes multi-layer ray map tokens to produce high-resolution point maps.

Training. To ensure our 3D latent space is decoupled from multi-view inputs and maintains view invariance, we employ a training strategy that samples data with varying resolutions, aspect ratios, and view counts N_{obs}. This enables our 3D latent tokens to represent 3D scenes under flexible observational configurations.

As for supervision, in addition to supervising rendered images with MSE and perceptual losses, we introduce an adversarial loss following common practices in 2D VAEs [63]. For the optional point map head, we adopt an aleatoric-uncertainty loss to weight the discrepancy between the predicted point map and ground truth. The overall training objective is:

$$\mathcal{L} = \text{MSE}(\hat{\mathbf{I}}^t, \mathbf{I}^t) + \lambda_1 \cdot \text{LPIPS}(\hat{\mathbf{I}}^t, \mathbf{I}^t) + \lambda_2 \cdot \omega_G \cdot \text{GAN}(\hat{\mathbf{I}}^t, \mathbf{I}^t) + \lambda_3 \cdot \mathcal{L}_{pmap}(\hat{\mathbf{P}}^t, \hat{\mathbf{C}}^t, \mathbf{P}^t), \tag{6}$$

where $\hat{\mathbf{I}}^t$ and $\mathbf{I}^t$ are the predicted and ground-truth images. $\hat{\mathbf{P}}^t$ and $\mathbf{P}^t$ denote the predicted and ground-truth point maps. $\hat{\mathbf{C}}^t$ denotes the uncertainty map. The definition of $\mathcal{L}_{pmap}$ follows VGGT [42].

3.3 3DDiT: Taming Diffusion Transformers for 3D-Grounded Generation

With the proposed 3DRAE capable of mapping any multi-view observed 3D scene into a compact 3D latent space, we now turn to modeling this space with a 3D diffusion transformer (3DDiT) for 3D-grounded generation. Our 3DDiT effectively learns to transform empty or partial 2D observations into complete 3D scene realizations by denoising in the 3D latent space.

Model Design. The architecture of our 3DDiT is shown in Fig.1-b. Following [1], we adopt the LightningDiT [64] backbone with wide diffusion head, scaling the DiT [65] width to match the high dimensionality of our 3D latent tokens. Unlike prior methods that sample from 2D latent tokens proportional to the number of views, our 3DDiT operates on the compact, fixed-length 3D latent tokens. Since the 3D latent space are comprehensively grounded in 3D via novel view synthesis and 3D reconstruction in our 3DRAE, it inherently yields better efficiency and spatial consistency.

Diverse Conditioning Configurations. Since our 3DRAE encoder can map varying number of images and their poses to the 3D latent space, we can leverage it to encode conditioning signals from observational views under diverse configurations for our 3DDiT. Particularly, we decompose conditioning into: (i) spatial extent specified by camera trajectory $\mathcal{P}_{\text{cond}} = \{P_i\}_{i=1}^{N_{\text{pose}}}$, and (ii) appearance specified by multi-view images $\mathcal{I}_{\text{cond}} = \{I_j\}_{j=1}^{N_{\text{img}}}$, where $N_{\text{pose}} \geq N_{\text{img}}$ since the camera trajectory should comprehensively covers the scene's spatial extent, while multi-view image observations may be partial or absent. As shown in Fig.1-b, we define three conditioning configurations:

- **Unconditioning** ($N_{\text{img}} = 0$): Only the camera trajectory $\mathcal{P}_{\text{cond}}$ is provided, defining the spatial scope without appearance constraints. The scene should be generated from scratch.
- **Single-view conditioning** ($N_{\text{img}} = 1$): In addition to the trajectory $\mathcal{P}_{\text{cond}}$, one reference image from a particular viewpoint is provided to guide appearance, demanding strong spatial completion to unobserved regions.
- **Sparse-view conditioning** ($N_{\text{img}} > 1$): In addition to the trajectory $\mathcal{P}_{\text{cond}}$, several images from multiple viewpoints are provided for appearance reference, requiring faithful reconstruction and cross-view spatial consistency.

To accommodate the case where $N_{\text{pose}} > N_{\text{img}}$, we introduce a random masking strategy (see details in A.4) when training 3DRAE to make it aware that some of the input views are invisible.

Flow Matching in 3D Latent Space. We adopt the flow matching framework [66, 67] to model the probability path of our 3D latent space. Given a clean latent $Z_0 \in \mathbb{R}^{m \times d}$ encoded by 3DRAE and a condition c comprising the partial observations $\mathcal{I}_{\text{cond}}$ and camera trajectory $\mathcal{P}_{\text{cond}}$, we construct a linearly interpolated probability path between Z_0 and Gaussian noise $\epsilon \sim \mathcal{N}(0, \mathbf{I})$:

$$Z_t = (1-t)Z_0 + t\epsilon, \quad \text{where } t \sim \mathcal{U}[0,1], \quad Z_t \in \mathbb{R}^{m \times d}. \tag{7}$$

The associated velocity field is $u_t = \epsilon - Z_0$. Our 3DDiT v_θ learns to predict this velocity conditioned on the noisy latent Z_t, timestep t, and condition c:

$$\mathcal{L}_{\text{FM}} = \mathbb{E}_{t, Z_0, \epsilon}\left[\|v_\theta(Z_t, t, c) - (\epsilon - Z_0)\|_2^2\right]. \tag{8}$$

4 Experiments

In this section, we present necessary implementation details in § 4.1, benchmark settings in § 4.2, as well as baseline and metric settings in § 4.3. Then we evaluate our method across various settings to demonstrate its effectiveness in § 4.4. We also present ablations and discussions in § 4.5. **Additional experimental details and results can be found in our Appendix and Supplementary Videos.**

4.1 Implementation Details

Our 3DRAE is trained on 32 A800 GPUs for 160k steps, using an 8k-step warm-up and a peak learning rate of 2×10^{-4}. Our 3DDiT is trained for 80k steps with the same hardware and learning rate schedule. To process multi-view image data, we follow large 3D reconstruction models[43, 68] and adopt a dynamic data sampling strategy, where the batch size is dynamically determined by the sampled resolution, aspect ratio, and number of views. In particular, for each GPU, the image resolution is randomized to fit the total pixel count between 37,000 and 75,500, the aspect ratio is randomly sampled from the range [0.7, 1.8], and the total number of views ranges from 6 to 18. During the training of 3DRAE, we randomly mask out input views with a probability of 0.1 and supervise the model solely with novel-view image and point map rendering. During the training of 3DDiT, we randomly mask out input views with a probability ranging from 0.6 to 0.9 to simulate varying conditional view counts, and mask out all views with a probability of 0.1 to accommodate unconditional generation. Such training strategy enables our method to support diverse conditioning configurations. Our 3DRAE and 3DDiT are trained on a large collection of 17 multi-view datasets (Table 7), spanning $\sim$130K scenes ranging from indoor to outdoor and from object-centric to general environments. Please refer to our Appendix for further implementation and data processing details.

4.2 Benchmark

To comprehensively evaluate our method across diverse settings, we collected 358 scenes in total from four datasets—DL3DV[69], RealEstate10K[70], CO3D[71] and ScanNet[72]. This collection covers a wide range of scenarios, from indoor to outdoor and from object-centric to general scenes. For each scene, we sample a trajectory from the original video that covers the main subject with substantial camera motion. We evaluate methods by predicting unseen views given only one or few conditional views. To assess performance under varying conditioning settings, we randomly sample different numbers of conditional views from the trajectory as reference. Fewer conditional views correspond to sparser observations, shifting the evaluation toward 3D generation capability; more conditional views correspond to denser observations emphasize 3D reconstruction fidelity.

4.3 Baselines and Metrics

Baselines. We compare our method against both regression-based (DepthSplat[36], LVSM[44]) and diffusion-based approaches (MotionCtrl[22], ViewCrafter[28], SEVA[27]). Regression-based methods excel at faithfully reconstructing 3D scenes under dense observation. Diffusion-based methods, by contrast, leverage the generative capabilities of video diffusion models and are better suited for completing unseen regions under partial observation. All methods follow their official implementations and are evaluated on our benchmark.

	Method	Runtime↓	DL3DV [69]					RE10K [70]				
			PSNR↑	LPIPS↓	FID↓	ATE_r ↓	ATE_t ↓	PSNR↑	LPIPS↓	FID↓	ATE_r ↓	ATE_t ↓
1-view	DepthSplat[36]	0.15s	9.11	0.631	141.14	1.27	0.155	11.65	0.584	113.03	0.85	0.102
	LVSM[44]	0.21s	14.58	0.581	114.83	1.64	0.197	17.42	0.385	30.94	0.55	0.077
	MotionCtrl[22]	11.8s	10.72	0.655	128.77	2.32	0.290	10.23	0.672	115.55	2.47	0.260
	ViewCrafter[28]	200.4s	9.31	0.667	94.08	1.58	0.196	13.77	0.454	55.88	1.08	0.110
	SEVA[27]	85.2s	14.60	0.511	45.96	0.32	0.029	15.52	0.426	27.21	0.28	0.021
	3DRAE (ours)	0.23s	14.07	0.520	84.67	1.33	0.127	14.95	0.466	30.48	0.80	0.070
	3DDiT (ours)	1.98s	14.62	0.480	40.93	0.29	0.025	15.77	0.411	24.67	0.26	0.021
2-view	DepthSplat[36]	0.16s	13.57	0.637	146.06	1.41	0.171	16.17	0.369	51.98	0.43	0.042
	LVSM[44]	0.23s	17.52	0.468	89.85	1.32	0.151	23.22	0.180	17.59	0.26	0.022
	MotionCtrl[22]	N/A	N/A	N/A	N/A	N/A	N/A	N/A	N/A	N/A	N/A	N/A
	ViewCrafter[28]	202.2s	12.57	0.560	117.94	1.59	0.200	15.36	0.429	57.31	0.83	0.089
	SEVA[27]	86.4s	16.22	0.433	35.96	0.31	0.033	19.44	0.260	18.30	0.28	0.021
	3DRAE (ours)	0.24s	17.19	0.374	37.07	0.47	0.060	19.57	0.256	15.99	0.19	0.019
	3DDiT (ours)	2.01s	15.95	0.415	33.15	0.27	0.023	18.19	0.298	17.70	0.18	0.015

	Method	Runtime↓	CO3D [71]					ScanNet [72]				
			PSNR↑	LPIPS↓	FID↓	ATE_r ↓	ATE_t ↓	PSNR↑	LPIPS↓	FID↓	ATE_r ↓	ATE_t ↓
1-view	DepthSplat[36]	0.15s	8.07	0.671	153.80	1.72	0.220	10.19	0.607	141.85	0.43	0.119
	LVSM[44]	0.21s	15.32	0.616	192.31	2.22	0.303	15.34	0.500	87.19	0.72	0.172
	MotionCtrl[22]	11.8s	11.35	0.673	124.90	2.25	0.432	10.04	0.672	149.80	2.09	0.325
	ViewCrafter[28]	200.4s	9.31	0.667	152.32	2.23	0.427	12.69	0.533	79.91	1.40	0.232
	SEVA[27]	85.2s	17.31	0.462	42.50	0.92	0.029	14.47	0.507	53.11	0.28	0.065
	3DRAE (ours)	0.23s	15.43	0.536	113.4	1.60	0.248	15.24	0.472	66.93	0.59	0.117
	3DDiT (ours)	1.98s	17.01	0.460	42.29	0.68	0.026	15.74	0.448	47.97	0.22	0.062
2-view	DepthSplat[36]	0.16s	15.74	0.616	146.01	1.71	0.281	15.31	0.472	104.97	0.70	0.114
	LVSM[44]	0.23s	16.87	0.569	167.60	2.19	0.359	20.04	0.323	54.89	0.33	0.087
	MotionCtrl[22]	N/A	N/A	N/A	N/A	N/A	N/A	N/A	N/A	N/A	N/A	N/A
	ViewCrafter[28]	202.2s	10.24	0.664	174.71	2.16	0.414	14.03	0.492	79.76	1.36	0.218
	SEVA[27]	86.4s	19.96	0.375	36.95	0.92	0.028	18.48	0.348	36.75	0.26	0.069
	3DRAE (ours)	0.24s	19.34	0.382	34.18	0.73	0.022	19.61	0.314	36.73	0.21	0.050
	3DDiT (ours)	2.01s	18.21	0.411	34.33	0.68	0.025	18.28	0.355	38.73	0.21	0.048

Table 1: **Quantitative Comparison.** We compare both generation-oriented (1-view) and reconstruction-oriented (2-view) settings with state-of-the-art regression-based (DepthSplat, LVSM) and diffusion-based (MotionCtrl, ViewCrafter, SEVA) methods. 2-view setting is not available (N/A) for MotionCtrl that only supports 1-view conditioning. PSNR and LPIPS are used for ***reconstruction-prioritized evaluation***. FID is used for ***generation-prioritized evaluation***. ATE_r and ATE_t are used for ***spatial consistency evaluation***.

Metrics. ***For reconstruction quality***, we adopt PSNR and LPIPS to measure photometric and perceptual differences between predicted and ground-truth images. ***For generation quality***, we use FID to quantify the distance between generated and real image distributions. ***To assess spatial consistency***, we follow prior work [28] to employ pose accuracy, where ATE_r and ATE_t denote rotation and translation errors between predicted and ground-truth camera poses. We note that PSNR and LPIPS are indicative only when scene observations are relatively complete (i.e., number of conditional views > 1). When conditioned on a single view, generated images increasingly involve content synthesized from scratch as the camera moves. In such cases, FID for image quality and pose accuracy for spatial consistency become more appropriate evaluation focuses.

4.4 Main Results

Quantitative Comparison. Our quantitative results are presented in Table 1. All methods are evaluated under both single-view and sparse-view conditioning settings. Runtime is computed as the average time cost to render 16 views, which exhibits minimal variation across different conditioning settings for all methods. Notably, our 3DDiT achieves substantially shorter runtime compared to all 2D diffusion-based approaches. This efficiency stems from denoising directly in a compact 3D latent space, which eliminates the representation redundancy introduced by 2D views. Our 3DRAE also matches regression-based methods in runtime. In terms of performance, when only single view is available for conditioning (1-view), our 3DDiT demonstrates clear superiority compared to all baselines across all datasets and metrics, especially in FID and pose accuracy, highlighting its advantages in generation quality and spatial consistency. For sparse-view conditioning (2-view, start-end-view) where reconstruction fidelity rather than generative diversity is prioritized, our 3DRAE sometimes outperforms 3DDiT. This is because 3DDiT is not designed for faithful reconstruction. The denoising process of diffusion transformer may cause generated scenes to deviate from conditional



Figure 4: **Qualitative Comparison. Top**: Comparison with state-of-the-art methods. **Bottom**: Comparison between our 3DRAE and 3DDiT to demonstrate the effectiveness of diffusion modeling, where 3DRAE fails in 1-view setting that prioritizes generation capability. The red bounding boxes highlight failure cases in baselines.

observations. Overall, the results show that both our 3DRAE and 3DDiT achieve competitive performance under sparse-view conditioning, demonstrating the effectiveness of our method.

Qualitative Comparison. We also present qualitative results in Fig.4 for more intuitive demonstration. *For 2D diffusion-based methods* (i.e., MotionCtrl[22], ViewCrafter[28], SEVA[27]), we focus on comparing generation quality and thus show results under single-view conditioning. Under large motion, MotionCtrl misaligns with target poses. ViewCrafter uses point cloud renderings as condition signals but suffers black holes from occluded regions. SEVA adds dense anchor frames, improving quality and adherence, yet images still deviate, blur, or have artifacts. In contrast, our 3DDiT consistently produces high-quality images that align accurately with target views. *For regression-based methods* (i.e., DepthSplat[36], LVSM[44]), the focus is reconstruction quality. We therefore present results with two views as conditioning. Despite overlap in conditional views, both DepthSplat and LVSM fail to handle large motion and occlusions, as they lack generative capabilities. In contrast, our method plausibly completes the occluded regions with superior rendering quality.

In the bottom of Fig.4, we further compare 3DRAE and 3DDiT under both generation-prioritized (1-view) and reconstruction-prioritized (6-view) settings. In 1-view setting, 3DRAE fails to extrapolate to unobserved regions, with quality deteriorating as viewpoint changes. 3DDiT, benefiting from diffusion modeling, generates plausible occluded regions while preserving spatial consistency. In 6-view setting, since the conditioning appearance is complete, both models perform well.

4.5 Discussions

Choices for 2D Foundation model. Since our 3DRAE derives 3D latent tokens from 2D representation models, we explore the impact on 3D reconstruction and generation by varying the 2D foundation model of 3DRAE and further yielding variants of 3DDiT. We also implement the variant (3DRAE-ImgOnly, 3DDiT-ImgOnly) without any representation model for reference, where we replace multi-view features derived from representation models with raw image patch embeddings in 3DRAE. For 3DRAE that prioritizes reconstruction, we evaluate the impact of 2D foundation model under 6-view conditioning, where observations are sufficiently dense. For 3DDiT that focuses on generation, we conduct analysis under 1-view conditioning, where most scene content need to be generated from scratch.

Split / 6-view	DL3DV [69]		RE10K [70]	
	PSNR↑	LPIPS↓	PSNR↑	LPIPS↓
3DRAE-ImgOnly	21.42	0.226	25.49	0.124
3DRAE-DA3[43]	21.62	0.221	26.38	0.118
3DRAE-SigLIP2[49]	19.40	0.283	22.60	0.187
3DRAE-DINOv2[48]	19.22	0.281	21.98	0.186

Split / 1-view	DL3DV [69]			RE10K [70]		
	FID↓	ATE_r ↓	ATE_t ↓	FID↓	ATE_r ↓	ATE_t ↓
3DDiT-ImgOnly	51.68	1.02	0.093	30.31	0.89	0.047
3DDiT-DA3[43]	47.75	0.54	0.057	29.76	0.66	0.034
3DDiT-SigLIP2[49]	44.65	0.32	0.029	26.74	0.29	0.024
3DDiT-DINOv2[48]	40.93	0.29	0.025	24.67	0.26	0.021

Table 2: **Ablation on 2D Foundation Model.**

Split / 6-view	Runtime↓	DL3DV [69]		RE10K [70]	
		PSNR↑	LPIPS↓	PSNR↑	LPIPS↓
3DRAE-tok256	0.10s	18.22	0.324	20.73	0.226
3DRAE-tok512	0.17s	18.76	0.301	21.36	0.207
3DRAE-tok1024	0.23s	19.22	0.281	21.98	0.186

Split / 1-view	Runtime↓	DL3DV [69]			RE10K [70]		
		FID↓	ATE_r ↓	ATE_t ↓	FID↓	ATE_r ↓	ATE_t ↓
3DDiT-XL-tok256	1.41s	42.02	0.31	0.025	25.47	0.28	0.022
3DDiT-XL-tok512	1.67s	41.85	0.30	0.027	25.12	0.28	0.021
3DDiT-S-tok1024	1.14s	44.83	0.33	0.031	28.31	0.46	0.027
3DDiT-B-tok1024	1.35s	42.83	0.32	0.029	26.83	0.38	0.025
3DDiT-XL-tok1024	1.98s	40.93	0.29	0.025	24.67	0.26	0.021

Table 3: **Ablation on Representation and Model Capacity.**

We report the results on DL3DV and RE10K datasets in Table 2. Among all 3DRAE variants, the one built upon DA3[43] achieves the best reconstruction performance, demonstrating that 3D prior knowledge from large multi-view reconstruction models benefits the reconstruction capability of 3D latent representation. In contrast, 3DRAEs built upon semantics-prioritized 2D representations (i.e., DINOv2[48], SigLIP2[49]) exhibits worse reconstruction fidelity, even underperforming the image-only baseline without any representation model. This implies that *high-level semantic representation is deficient in faithful reconstruction*, consistent with findings in 2DRAEs[1] where variants based on DINOv2/SigLIP2 underperform those based on reconstruction-focused models like MAE[57]. For 3DDiT, the results reveals a striking reversal. Surprisingly, variants built upon DINOv2 and SigLIP2 achieve substantially better generation quality and spatial consistency than their DA3-based and image-only counterparts, suggesting that *semantic priors are crucial for enhancing 3D generation*. Qualitative results in Fig.5 further support this finding: DA3-based and image-only 3DDiTs fail to learn general scene appearance, wheareas DINOv2 and SigLIP2-based models generate plausible appearance. Since this work is centered on 3D generation, we default to DINOv2 as our 2D encoder for the best generation performance.



Figure 5: **Qualitative Ablations on 2D Foundation Models.**

Scaling with Capacity. We further evaluate the scalability of both 3DRAE and 3DDiT with respect to representation capacity (i.e., the number of 3D latent tokens) and model capacity (i.e., the size of 3DDiT model). Following the same protocol as Table 2, we report reconstruction and generation results under their respective evaluation settings in Table 3. We can see that while reducing the number of 3D latent tokens significantly degrades 3DRAE reconstruction fidelity, the resulting more compact 3D latent space benefits diffusion modeling—such that the generation quality does not deteriorate sharply with fewer tokens. Notably, *our 3DDiT with 256 tokens achieves highly competitive generation performance while offering substantially better efficiency.* Furthermore, generation quality scales positively with 3DDiT model size, demonstrating the scalability of our method with the number of parameters.

Split / 1-view	DL3DV [69]	RE10K [70]
	FID↓	FID↓
3DDiT-w/o IN	43.15	26.15
3DDiT-w/ IN	**40.93**	**24.67**

Table 4: **Ablation on ImageNet (IN) pre-training.**

Compatibility with Single-Image Data. Since our 3DRAE can lift an arbitrary number of views—including a single image—to the 3D latent space, we can leverage single-image data during 3DDiT pre-training as described in § 3.3. As shown in Table 4, benefiting from the diversity and scale of ImageNet [73], pre-training equips our 3DDiT with general scene appearance priors and improves generation quality. This highlights the compatibility of our approach with single-image data and its potential to scale to massive 2D image and video datasets.

5 Conclusion

In this paper, we propose a novel approach that performs diffusion modeling directly within an compact and implicit 3D latent space. Our method grounds semantic representations from frozen 2D foundation models with explicit 3D awareness, transforming 2D features that scale linearly with the number of views into view-invariant 3D latent tokens. A diffusion transformer is then built upon this 3D latent space, enabling 3D scene generation with superior efficiency and spatial consistency compared to prior 2D-based approaches. Furthermore, we comprehensively investigate the impact of 2D foundation model on 3D generation performance and reveal that semantic prior knowledge substantially benefits generation quality. Finally, we validate the scalability of our model with respect to both representation capacity and model size, demonstrating the strong potential of our approach for scaling up to broader model regimes.

Limitations. In this paper, we train our model on as many large-scale multi-view datasets as we can access, and demonstrate the strong generalization ability of the proposed 3D latent representation for out-of-distribution 3D scene reconstruction and generation. Our method also shows significant potential to outperform 2D diffusion-based approaches in both efficiency and spatial consistency. Nevertheless, compared to the 2D image and video generation models developed by well-resourced industrial groups—which are trained on web-scale image and video data, often supplemented with large amounts of proprietary in-house data—the scale of our training data remains relatively limited. To fully unlock the potential of 3D latent representation for 3D scene generation, it is necessary to further scale up the data volume by leveraging massive Internet image and video data, thereby improving the fundamental capabilities of the model.

Acknowledgments

This work was supported in part by NSFC under Grant 62202389, in part by a grant from the Westlake University-Muyuan Joint Research Institute, in part by the Westlake Education Foundation, and in part by the Open Project Program of the State Key Laboratory of CAD&CG (Grant No. A2513), Zhejiang University.

References

[1] Boyang Zheng, Nanye Ma, Shengbang Tong, and Saining Xie. Diffusion transformers with representation autoencoders. *arXiv preprint arXiv:2510.11690*, 2025.

[2] Eric R Chan, Connor Z Lin, Matthew A Chan, Koki Nagano, Boxiao Pan, Shalini De Mello, Orazio Gallo, Leonidas J Guibas, Jonathan Tremblay, Sameh Khamis, et al. Efficient geometry-aware 3d generative adversarial networks. In *Proceedings of the IEEE/CVF conference on computer vision and pattern recognition*, pages 16123–16133, 2022.

[3] Miguel Angel Bautista, Pengsheng Guo, Samira Abnar, Walter Talbott, Alexander Toshev, Zhuoyuan Chen, Laurent Dinh, Shuangfei Zhai, Hanlin Goh, Daniel Ulbricht, et al. Gaudi: A neural architect for immersive 3d scene generation. *Advances in Neural Information Processing Systems*, 35:25102–25116, 2022.

[4] Hansheng Chen, Jiatao Gu, Anpei Chen, Wei Tian, Zhuowen Tu, Lingjie Liu, and Hao Su. Single-stage diffusion nerf: A unified approach to 3d generation and reconstruction. In *Proceedings of the IEEE/CVF international conference on computer vision*, pages 2416–2425, 2023.

[5] Philipp Henzler, Niloy J Mitra, and Tobias Ritschel. Escaping plato's cave: 3d shape from adversarial rendering. In *Proceedings of the IEEE/CVF International Conference on Computer Vision*, pages 9984–9993, 2019.

[6] Thu Nguyen-Phuoc, Chuan Li, Lucas Theis, Christian Richardt, and Yong-Liang Yang. Hologan: Unsupervised learning of 3d representations from natural images. In *Proceedings of the IEEE/CVF international conference on computer vision*, pages 7588–7597, 2019.

[7] Thu H Nguyen-Phuoc, Christian Richardt, Long Mai, Yongliang Yang, and Niloy Mitra. Blockgan: Learning 3d object-aware scene representations from unlabelled images. *Advances in neural information processing systems*, 33:6767–6778, 2020.

[8] Animesh Karnewar, Andrea Vedaldi, David Novotny, and Niloy J Mitra. Holodiffusion: Training a 3d diffusion model using 2d images. In *Proceedings of the IEEE/CVF conference on computer vision and pattern recognition*, pages 18423–18433, 2023.

[9] Katja Schwarz, Yiyi Liao, Michael Niemeyer, and Andreas Geiger. Graf: Generative radiance fields for 3d-aware image synthesis. *Advances in neural information processing systems*, 33:20154–20166, 2020.

[10] Michael Niemeyer and Andreas Geiger. Giraffe: Representing scenes as compositional generative neural feature fields. In *Proceedings of the IEEE/CVF conference on computer vision and pattern recognition*, pages 11453–11464, 2021.

[11] Seung Wook Kim, Bradley Brown, Kangxue Yin, Karsten Kreis, Katja Schwarz, Daiqing Li, Robin Rombach, Antonio Torralba, and Sanja Fidler. Neuralfield-ldm: Scene generation with hierarchical latent diffusion models. In *Proceedings of the IEEE/CVF conference on computer vision and pattern recognition*, pages 8496–8506, 2023.

[12] Robin Rombach, Andreas Blattmann, Dominik Lorenz, Patrick Esser, and Björn Ommer. High-resolution image synthesis with latent diffusion models. In *Proceedings of the IEEE/CVF conference on computer vision and pattern recognition*, pages 10684–10695, 2022.

[13] Andreas Blattmann, Tim Dockhorn, Sumith Kulal, Daniel Mendelevitch, Maciej Kilian, Dominik Lorenz, Yam Levi, Zion English, Vikram Voleti, Adam Letts, et al. Stable video diffusion: Scaling latent video diffusion models to large datasets. *arXiv preprint arXiv:2311.15127*, 2023.

[14] Jonathan Ho, Tim Salimans, Alexey Gritsenko, William Chan, Mohammad Norouzi, and David J Fleet. Video diffusion models. *Advances in neural information processing systems*, 35:8633–8646, 2022.

[15] Zhuoyi Yang, Jiayan Teng, Wendi Zheng, Ming Ding, Shiyu Huang, Jiazheng Xu, Yuanming Yang, Wenyi Hong, Xiaohan Zhang, Guanyu Feng, et al. Cogvideox: Text-to-video diffusion models with an expert transformer. *arXiv preprint arXiv:2408.06072*, 2024.

[16] Weijie Kong, Qi Tian, Zijian Zhang, Rox Min, Zuozhuo Dai, Jin Zhou, Jiangfeng Xiong, Xin Li, Bo Wu, Jianwei Zhang, et al. Hunyuanvideo: A systematic framework for large video generative models. *arXiv preprint arXiv:2412.03603*, 2024.

[17] Haoxin Chen, Yong Zhang, Xiaodong Cun, Menghan Xia, Xintao Wang, Chao Weng, and Ying Shan. Videocrafter2: Overcoming data limitations for high-quality video diffusion models. In *Proceedings of the IEEE/CVF conference on computer vision and pattern recognition*, pages 7310–7320, 2024.

[18] Team Wan, Ang Wang, Baole Ai, Bin Wen, Chaojie Mao, Chen-Wei Xie, Di Chen, Feiwu Yu, Haiming Zhao, Jianxiao Yang, et al. Wan: Open and advanced large-scale video generative models. *arXiv preprint arXiv:2503.20314*, 2025.

[19] Ruiqi Gao, Aleksander Holynski, Philipp Henzler, Arthur Brussee, Ricardo Martin-Brualla, Pratul Srinivasan, Jonathan T Barron, and Ben Poole. Cat3d: Create anything in 3d with multi-view diffusion models. *arXiv preprint arXiv:2405.10314*, 2024.

[20] Xinyang Li, Zhangyu Lai, Linning Xu, Yansong Qu, Liujuan Cao, Shengchuan Zhang, Bo Dai, and Rongrong Ji. Director3d: Real-world camera trajectory and 3d scene generation from text. *Advances in neural information processing systems*, 37:75125–75151, 2024.

[21] Yuanbo Yang, Jiahao Shao, Xinyang Li, Yujun Shen, Andreas Geiger, and Yiyi Liao. Prometheus: 3d-aware latent diffusion models for feed-forward text-to-3d scene generation. In *Proceedings of the IEEE/CVF Conference on Computer Vision and Pattern Recognition*, pages 2857–2869, 2025.

[22] Zhouxia Wang, Ziyang Yuan, Xintao Wang, Yaowei Li, Tianshui Chen, Menghan Xia, Ping Luo, and Ying Shan. Motionctrl: A unified and flexible motion controller for video generation. In *ACM SIGGRAPH 2024 Conference Papers*, pages 1–11, 2024.

[23] Hyojun Go, Byeongjun Park, Jiho Jang, Jin-Young Kim, Soonwoo Kwon, and Changick Kim. Splatflow: Multi-view rectified flow model for 3d gaussian splatting synthesis. In *Proceedings of the Computer Vision and Pattern Recognition Conference*, pages 21524–21536, 2025.

[24] Hong-Xing Yu, Haoyi Duan, Charles Herrmann, William T Freeman, and Jiajun Wu. Wonderworld: Interactive 3d scene generation from a single image. In *Proceedings of the Computer Vision and Pattern Recognition Conference*, pages 5916–5926, 2025.

[25] Hanwen Liang, Junli Cao, Vidit Goel, Guocheng Qian, Sergei Korolev, Demetri Terzopoulos, Konstantinos N Plataniotis, Sergey Tulyakov, and Jian Ren. Wonderland: Navigating 3d scenes from a single image. In *Proceedings of the Computer Vision and Pattern Recognition Conference*, pages 798–810, 2025.

[26] Tianyu Huang, Wangguandong Zheng, Tengfei Wang, Yuhao Liu, Zhenwei Wang, Junta Wu, Jie Jiang, Hui Li, Rynson Lau, Wangmeng Zuo, et al. Voyager: Long-range and world-consistent video diffusion for explorable 3d scene generation. *ACM Transactions on Graphics (TOG)*, 44(6):1–15, 2025.

[27] Jensen Zhou, Hang Gao, Vikram Voleti, Aaryaman Vasishta, Chun-Han Yao, Mark Boss, Philip Torr, Christian Rupprecht, and Varun Jampani. Stable virtual camera: Generative view synthesis with diffusion models. In *Proceedings of the IEEE/CVF International Conference on Computer Vision*, pages 12405–12414, 2025.

[28] Wangbo Yu, Jinbo Xing, Li Yuan, Wenbo Hu, Xiaoyu Li, Zhipeng Huang, Xiangjun Gao, Tien-Tsin Wong, Ying Shan, and Yonghong Tian. Viewcrafter: Taming video diffusion models for high-fidelity novel view synthesis. *arXiv preprint arXiv:2409.02048*, 2024.

[29] Luxi Chen, Zihan Zhou, Min Zhao, Yikai Wang, Ge Zhang, Wenhao Huang, Hao Sun, Ji-Rong Wen, and Chongxuan Li. Flexworld: Progressively expanding 3d scenes for flexiable-view synthesis. *arXiv preprint arXiv:2503.13265*, 2025.

[30] Runjia Li, Philip Torr, Andrea Vedaldi, and Tomas Jakab. Vmem: Consistent interactive video scene generation with surfel-indexed view memory. In *Proceedings of the IEEE/CVF International Conference on Computer Vision*, pages 25690–25699, 2025.

[31] Qianqian Wang, Zhicheng Wang, Kyle Genova, Pratul P Srinivasan, Howard Zhou, Jonathan T Barron, Ricardo Martin-Brualla, Noah Snavely, and Thomas Funkhouser. Ibrnet: Learning multi-view image-based rendering. In *Proceedings of the IEEE/CVF conference on computer vision and pattern recognition*, pages 4690–4699, 2021.

[32] Jiaxiang Tang, Zhaoxi Chen, Xiaokang Chen, Tengfei Wang, Gang Zeng, and Ziwei Liu. Lgm: Large multi-view gaussian model for high-resolution 3d content creation. In *European Conference on Computer Vision*, pages 1–18. Springer, 2024.

[33] David Charatan, Sizhe Lester Li, Andrea Tagliasacchi, and Vincent Sitzmann. pixelsplat: 3d gaussian splats from image pairs for scalable generalizable 3d reconstruction. In *Proceedings of the IEEE/CVF conference on computer vision and pattern recognition*, pages 19457–19467, 2024.

[34] Kai Zhang, Sai Bi, Hao Tan, Yuanbo Xiangli, Nanxuan Zhao, Kalyan Sunkavalli, and Zexiang Xu. Gs-lrm: Large reconstruction model for 3d gaussian splatting. In *European Conference on Computer Vision*, pages 1–19. Springer, 2024.

[35] Yuedong Chen, Haofei Xu, Chuanxia Zheng, Bohan Zhuang, Marc Pollefeys, Andreas Geiger, Tat-Jen Cham, and Jianfei Cai. Mvsplat: Efficient 3d gaussian splatting from sparse multi-view images. In *European conference on computer vision*, pages 370–386. Springer, 2024.

[36] Haofei Xu, Songyou Peng, Fangjinhua Wang, Hermann Blum, Daniel Barath, Andreas Geiger, and Marc Pollefeys. Depthsplat: Connecting gaussian splatting and depth. In *Proceedings of the Computer Vision and Pattern Recognition Conference*, pages 16453–16463, 2025.

[37] Botao Ye, Sifei Liu, Haofei Xu, Xueting Li, Marc Pollefeys, Ming-Hsuan Yang, and Songyou Peng. No pose, no problem: Surprisingly simple 3d gaussian splats from sparse unposed images. *arXiv preprint arXiv:2410.24207*, 2024.

[38] Dongxu Wei, Zhiqi Li, and Peidong Liu. Omni-scene: Omni-gaussian representation for ego-centric sparse-view scene reconstruction. In *Proceedings of the Computer Vision and Pattern Recognition Conference*, pages 22317–22327, 2025.

[39] Qi Xu, Dongxu Wei, Lingzhe Zhao, Wenpu Li, Zhangchi Huang, Shunping Ji, and Peidong Liu. Siu3r: Simultaneous scene understanding and 3d reconstruction beyond feature alignment. In *The Thirty-ninth Annual Conference on Neural Information Processing Systems*, 2025.

[40] Shuzhe Wang, Vincent Leroy, Yohann Cabon, Boris Chidlovskii, and Jerome Revaud. Dust3r: Geometric 3d vision made easy. In *Proceedings of the IEEE/CVF conference on computer vision and pattern recognition*, pages 20697–20709, 2024.

[41] Vincent Leroy, Yohann Cabon, and Jérôme Revaud. Grounding image matching in 3d with mast3r. In *European conference on computer vision*, pages 71–91. Springer, 2024.

[42] Jianyuan Wang, Minghao Chen, Nikita Karaev, Andrea Vedaldi, Christian Rupprecht, and David Novotny. Vggt: Visual geometry grounded transformer. In *Proceedings of the Computer Vision and Pattern Recognition Conference*, pages 5294–5306, 2025.

[43] Haotong Lin, Sili Chen, Junhao Liew, Donny Y Chen, Zhenyu Li, Guang Shi, Jiashi Feng, and Bingyi Kang. Depth anything 3: Recovering the visual space from any views. *arXiv preprint arXiv:2511.10647*, 2025.

[44] Haian Jin, Hanwen Jiang, Hao Tan, Kai Zhang, Sai Bi, Tianyuan Zhang, Fujun Luan, Noah Snavely, and Zexiang Xu. Lvsm: A large view synthesis model with minimal 3d inductive bias. *arXiv preprint arXiv:2410.17242*, 2024.

[45] Qianqian Wang, Yifei Zhang, Aleksander Holynski, Alexei A Efros, and Angjoo Kanazawa. Continuous 3d perception model with persistent state. In *Proceedings of the Computer Vision and Pattern Recognition Conference*, pages 10510–10522, 2025.

[46] Hanwen Jiang, Hao Tan, Peng Wang, Haian Jin, Yue Zhao, Sai Bi, Kai Zhang, Fujun Luan, Kalyan Sunkavalli, Qixing Huang, et al. Rayzer: A self-supervised large view synthesis model. In *Proceedings of the IEEE/CVF International Conference on Computer Vision*, pages 4918–4929, 2025.

[47] Boyang Zheng, Nanye Ma, Shengbang Tong, and Saining Xie. Diffusion transformers with representation autoencoders, 2025.

[48] Maxime Oquab, Timothée Darcet, Théo Moutakanni, Huy Vo, Marc Szafraniec, Vasil Khalidov, Pierre Fernandez, Daniel Haziza, Francisco Massa, Alaaeldin El-Nouby, et al. Dinov2: Learning robust visual features without supervision. *arXiv preprint arXiv:2304.07193*, 2023.

[49] Michael Tschannen, Alexey Gritsenko, Xiao Wang, Muhammad Ferjad Naeem, Ibrahim Alabdulmohsin, Nikhil Parthasarathy, Talfan Evans, Lucas Beyer, Ye Xia, Basil Mustafa, et al. Siglip 2: Multilingual vision-language encoders with improved semantic understanding, localization, and dense features. *arXiv preprint arXiv:2502.14786*, 2025.

[50] Jiaxin Huang, Yuanbo Yang, Bangbang Yang, Lin Ma, Yuewen Ma, and Yiyi Liao. Gen3r: 3d scene generation meets feed-forward reconstruction. *arXiv preprint arXiv:2601.04090*, 2026.

[51] Zibo Zhao, Zeqiang Lai, Qingxiang Lin, Yunfei Zhao, Haolin Liu, Shuhui Yang, Yifei Feng, Mingxin Yang, Sheng Zhang, Xianghui Yang, et al. Hunyuan3d 2.0: Scaling diffusion models for high resolution textured 3d assets generation. *arXiv preprint arXiv:2501.12202*, 2025.

[52] Jianfeng Xiang, Xiaoxue Chen, Sicheng Xu, Ruicheng Wang, Zelong Lv, Yu Deng, Hongyuan Zhu, Yue Dong, Hao Zhao, Nicholas Jing Yuan, et al. Native and compact structured latents for 3d generation. *arXiv preprint arXiv:2512.14692*, 2025.

[53] Jingfeng Yao, Bin Yang, and Xinggang Wang. Reconstruction vs. generation: Taming optimization dilemma in latent diffusion models. In *Proceedings of the Computer Vision and Pattern Recognition Conference*, pages 15703–15712, 2025.

[54] Hao Chen, Yujin Han, Fangyi Chen, Xiang Li, Yidong Wang, Jindong Wang, Ze Wang, Zicheng Liu, Difan Zou, and Bhiksha Raj. Masked autoencoders are effective tokenizers for diffusion models. In *Forty-second International Conference on Machine Learning*, 2025.

[55] Junyu Chen, Dongyun Zou, Wenkun He, Junsong Chen, Enze Xie, Song Han, and Han Cai. Dc-ae 1.5: Accelerating diffusion model convergence with structured latent space. In *Proceedings of the IEEE/CVF International Conference on Computer Vision*, pages 19628–19637, 2025.

[56] Jiawei Yang, Tianhong Li, Lijie Fan, Yonglong Tian, and Yue Wang. Latent denoising makes good visual tokenizers. *arXiv preprint arXiv:2507.15856*, 2025.

[57] Kaiming He, Xinlei Chen, Saining Xie, Yanghao Li, Piotr Dollár, and Ross Girshick. Masked autoencoders are scalable vision learners. In *Proceedings of the IEEE/CVF conference on computer vision and pattern recognition*, pages 16000–16009, 2022.

[58] Sihyun Yu, Sangkyung Kwak, Huiwon Jang, Jongheon Jeong, Jonathan Huang, Jinwoo Shin, and Saining Xie. Representation alignment for generation: Training diffusion transformers is easier than you think. *arXiv preprint arXiv:2410.06940*, 2024.

[59] Shuai Wang, Zhi Tian, Weilin Huang, and Limin Wang. Ddt: Decoupled diffusion transformer. *arXiv preprint arXiv:2504.05741*, 2025.

[60] Ge Wu, Shen Zhang, Ruijing Shi, Shanghua Gao, Zhenyuan Chen, Lei Wang, Zhaowei Chen, Hongcheng Gao, Yao Tang, Jian Yang, et al. Representation entanglement for generation: Training diffusion transformers is much easier than you think. *arXiv preprint arXiv:2507.01467*, 2025.

[61] Kexun Zhang, Xianjun Yang, William Yang Wang, and Lei Li. Redi: efficient learning-free diffusion inference via trajectory retrieval. In *International Conference on Machine Learning*, pages 41770–41785. PMLR, 2023.

[62] René Ranftl, Alexey Bochkovskiy, and Vladlen Koltun. Vision transformers for dense prediction. In *Proceedings of the IEEE/CVF international conference on computer vision*, pages 12179–12188, 2021.

[63] Anders Boesen Lindbo Larsen, Søren Kaae Sønderby, Hugo Larochelle, and Ole Winther. Autoencoding beyond pixels using a learned similarity metric. In *International conference on machine learning*, pages 1558–1566. PMLR, 2016.

[64] Jingfeng Yao, Bin Yang, and Xinggang Wang. Reconstruction vs. generation: Taming optimization dilemma in latent diffusion models. In *Proceedings of the Computer Vision and Pattern Recognition Conference*, pages 15703–15712, 2025.

[65] William Peebles and Saining Xie. Scalable diffusion models with transformers. In *Proceedings of the IEEE/CVF international conference on computer vision*, pages 4195–4205, 2023.

[66] Yaron Lipman, Ricky TQ Chen, Heli Ben-Hamu, Maximilian Nickel, and Matt Le. Flow matching for generative modeling. *arXiv preprint arXiv:2210.02747*, 2022.

[67] Xingchao Liu, Chengyue Gong, and Qiang Liu. Flow straight and fast: Learning to generate and transfer data with rectified flow. *arXiv preprint arXiv:2209.03003*, 2022.

[68] Yifan Wang, Jianjun Zhou, Haoyi Zhu, Wenzheng Chang, Yang Zhou, Zizun Li, Junyi Chen, Jiangmiao Pang, Chunhua Shen, and Tong He. pi3: Permutation-equivariant visual geometry learning. *arXiv preprint arXiv:2507.13347*, 2025.

[69] Lu Ling, Yichen Sheng, Zhi Tu, Wentian Zhao, Cheng Xin, Kun Wan, Lantao Yu, Qianyu Guo, Zixun Yu, Yawen Lu, et al. Dl3dv-10k: A large-scale scene dataset for deep learning-based 3d vision. In *Proceedings of the IEEE/CVF Conference on Computer Vision and Pattern Recognition*, pages 22160–22169, 2024.

[70] Tinghui Zhou, Richard Tucker, John Flynn, Graham Fyffe, and Noah Snavely. Stereo magnification: Learning view synthesis using multiplane images. *ACM Trans. Graph. (Proc. SIGGRAPH)*, 37, 2018.

[71] Jeremy Reizenstein, Roman Shapovalov, Philipp Henzler, Luca Sbordone, Patrick Labatut, and David Novotny. Common objects in 3d: Large-scale learning and evaluation of real-life 3d category reconstruction. In *Proceedings of the IEEE/CVF international conference on computer vision*, pages 10901–10911, 2021.

[72] Angela Dai, Angel X Chang, Manolis Savva, Maciej Halber, Thomas Funkhouser, and Matthias Nießner. Scannet: Richly-annotated 3d reconstructions of indoor scenes. In *Proceedings of the IEEE conference on computer vision and pattern recognition*, pages 5828–5839, 2017.

[73] Olga Russakovsky, Jia Deng, Hao Su, Jonathan Krause, Sanjeev Satheesh, Sean Ma, Zhiheng Huang, Andrej Karpathy, Aditya Khosla, Michael Bernstein, et al. Imagenet large scale visual recognition challenge. *International journal of computer vision*, 115(3):211–252, 2015.

[74] Patrick Esser, Sumith Kulal, Andreas Blattmann, Rahim Entezari, Jonas Müller, Harry Saini, Yam Levi, Dominik Lorenz, Axel Sauer, Frederic Boesel, et al. Scaling rectified flow transformers for high-resolution image synthesis. In *Forty-first international conference on machine learning*, 2024.

[75] Hongchi Xia, Yang Fu, Sifei Liu, and Xiaolong Wang. Rgbd objects in the wild: Scaling real-world 3d object learning from rgb-d videos, 2024.

[76] Gilad Baruch, Zhuoyuan Chen, Afshin Dehghan, Tal Dimry, Yuri Feigin, Peter Fu, Thomas Gebauer, Brandon Joffe, Daniel Kurz, Arik Schwartz, et al. Arkitscenes: A diverse real-world dataset for 3d indoor scene understanding using mobile rgb-d data. *arXiv preprint arXiv:2111.08897*, 2021.

[77] Chandan Yeshwanth, Yueh-Cheng Liu, Matthias Nießner, and Angela Dai. Scannet++: A high-fidelity dataset of 3d indoor scenes. In *Proceedings of the IEEE/CVF International Conference on Computer Vision*, pages 12–22, 2023.

[78] Amir R Zamir, Alexander Sax, William Shen, Leonidas J Guibas, Jitendra Malik, and Silvio Savarese. Taskonomy: Disentangling task transfer learning. In *Proceedings of the IEEE conference on computer vision and pattern recognition*, pages 3712–3722, 2018.

[79] Santhosh K Ramakrishnan, Aaron Gokaslan, Erik Wijmans, Oleksandr Maksymets, Alex Clegg, John Turner, Eric Undersander, Wojciech Galuba, Andrew Westbury, Angel X Chang, et al. Habitat-matterport 3d dataset (hm3d): 1000 large-scale 3d environments for embodied ai. *arXiv preprint arXiv:2109.08238*, 2021.

[80] Mike Roberts, Jason Ramapuram, Anurag Ranjan, Atulit Kumar, Miguel Angel Bautista, Nathan Paczan, Russ Webb, and Joshua M Susskind. Hypersim: A photorealistic synthetic dataset for holistic indoor scene understanding. In *Proceedings of the IEEE/CVF international conference on computer vision*, pages 10912–10922, 2021.

[81] Pei Sun, Henrik Kretzschmar, Xerxes Dotiwalla, Aurelien Chouard, Vijaysai Patnaik, Paul Tsui, James Guo, Yin Zhou, Yuning Chai, Benjamin Caine, et al. Scalability in perception for autonomous driving: Waymo open dataset. In *Proceedings of the IEEE/CVF conference on computer vision and pattern recognition*, pages 2446–2454, 2020.

[82] Gerhard Neuhold, Tobias Ollmann, Samuel Rota Bulo, and Peter Kontschieder. The mapillary vistas dataset for semantic understanding of street scenes. In *Proceedings of the IEEE international conference on computer vision*, pages 4990–4999, 2017.

[83] Yohann Cabon, Naila Murray, and Martin Humenberger. Virtual kitti 2. *arXiv preprint arXiv:2001.10773*, 2020.

[84] Po-Han Huang, Kevin Matzen, Johannes Kopf, Narendra Ahuja, and Jia-Bin Huang. Deepmvs: Learning multi-view stereopsis. In *IEEE Conference on Computer Vision and Pattern Recognition (CVPR)*, 2018.

[85] Yao Yao, Zixin Luo, Shiwei Li, Jingyang Zhang, Yufan Ren, Lei Zhou, Tian Fang, and Long Quan. Blendedmvs: A large-scale dataset for generalized multi-view stereo networks. In *Proceedings of the IEEE/CVF conference on computer vision and pattern recognition*, pages 1790–1799, 2020.

[86] Zhengqi Li and Noah Snavely. Megadepth: Learning single-view depth prediction from internet photos. In *Computer Vision and Pattern Recognition (CVPR)*, 2018.

[87] Wenshan Wang, Delong Zhu, Xiangwei Wang, Yaoyu Hu, Yuheng Qiu, Chen Wang, Yafei Hu, Ashish Kapoor, and Sebastian Scherer. Tartanair: A dataset to push the limits of visual slam. 2020.

[88] Ruicheng Wang, Sicheng Xu, Yue Dong, Yu Deng, Jianfeng Xiang, Zelong Lv, Guangzhong Sun, Xin Tong, and Jiaolong Yang. Moge-2: Accurate monocular geometry with metric scale and sharp details. *arXiv preprint arXiv:2507.02546*, 2025.

[89] Jürgen Sturm, Nikolas Engelhard, Felix Endres, Wolfram Burgard, and Daniel Cremers. A benchmark for the evaluation of rgb-d slam systems. In *2012 IEEE/RSJ international conference on intelligent robots and systems*, pages 573–580. IEEE, 2012.

[90] Zichao Zhang and Davide Scaramuzza. A tutorial on quantitative trajectory evaluation for visual (-inertial) odometry. In *2018 IEEE/RSJ international conference on intelligent robots and systems (IROS)*, pages 7244–7251. IEEE, 2018.

[91] Richard Hartley and Andrew Zisserman. *Multiple view geometry in computer vision*. Cambridge university press, 2003.

[92] Arno Knapitsch, Jaesik Park, Qian-Yi Zhou, and Vladlen Koltun. Tanks and temples: Benchmarking large-scale scene reconstruction. *ACM Transactions on Graphics*, 36(4), 2017.

[93] Jonathan T. Barron, Ben Mildenhall, Dor Verbin, Pratul P. Srinivasan, and Peter Hedman. Mip-nerf 360: Unbounded anti-aliased neural radiance fields. *CVPR*, 2022.

[94] Henrik Aanæs, Rasmus Ramsbøl Jensen, George Vogiatzis, Engin Tola, and Anders Bjorholm Dahl. Large-scale data for multiple-view stereopsis. *International Journal of Computer Vision*, 120(2):153–168, 2016.

[95] Shuai Bai, Keqin Chen, Xuejing Liu, Jialin Wang, Wenbin Ge, Sibo Song, Kai Dang, Peng Wang, Shijie Wang, Jun Tang, Humen Zhong, Yuanzhi Zhu, Mingkun Yang, Zhaohai Li, Jianqiang Wan, Pengfei Wang, Wei Ding, Zheren Fu, Yiheng Xu, Jiabo Ye, Xi Zhang, Tianbao Xie, Zesen Cheng, Hang Zhang, Zhibo Yang, Haiyang Xu, and Junyang Lin. Qwen2.5-vl technical report, 2025.

[96] Shuai Bai, Yuxuan Cai, Ruizhe Chen, Keqin Chen, Xionghui Chen, Zesen Cheng, Lianghao Deng, Wei Ding, Chang Gao, Chunjiang Ge, et al. Qwen3-vl technical report. *arXiv preprint arXiv:2511.21631*, 2025.

[97] Zhiwen Fan, Jian Zhang, Renjie Li, Junge Zhang, Runjin Chen, Hezhen Hu, Kevin Wang, Huaizhi Qu, Dilin Wang, Zhicheng Yan, et al. Vlm-3r: Vision-language models augmented with instruction-aligned 3d reconstruction. *arXiv preprint arXiv:2505.20279*, 2025.

[98] Diankun Wu, Fangfu Liu, Yi-Hsin Hung, and Yueqi Duan. Spatial-mllm: Boosting mllm capabilities in visual-based spatial intelligence. *arXiv preprint arXiv:2505.23747*, 2025.

[99] Jiahui Zhang, Yurui Chen, Yanpeng Zhou, Yueming Xu, Ze Huang, Jilin Mei, Junhui Chen, Yu-Jie Yuan, Xinyue Cai, Guowei Huang, et al. From flatland to space: Teaching vision-language models to perceive and reason in 3d. *arXiv preprint arXiv:2503.22976*, 2025.

[100] Duo Zheng, Shijia Huang, Yanyang Li, and Liwei Wang. Learning from videos for 3d world: Enhancing mllms with 3d vision geometry priors. *arXiv preprint arXiv:2505.24625*, 2025.

Appendix

A 3DRAE Implementation

The overall architecture detail and hyperparameter settings for all 3DRAE variants are presented in Table 5. In general, our 3DRAE is trained on a large collection of multi-view datasets for 120k steps, the discriminator is not trained until 50k steps, and the adversarial loss is not enabled until 60k steps. By default, we use DINOv2[48] as the frozen 2D encoder in our 3DRAE for all experiments if not otherwise specified. The hyperparameters for the dynamic data sampling and random masking strategy are presented in Table 5(b). In the following sections, we describe the settings in detail for each module separately.

(a) Network Architecture		
Frozen 2D Encoder	**DepthAnything3 (DA3) [43]**	
	Model Config	ViT-Base
	Patch Size	14
	Hidden Dim	768
	DINOv2 [48]	
	Model Config	ViT-Base
	Patch Size	14
	Hidden Dim	768
	SigLIP2 [49]	
	Model Config	ViT-Base
	Patch Size	16
	Hidden Dim	768
Ray Map Embedding	Input Channel	6+1=7
	Patch Size	14
	Embed Dim	768
	Conv Kernel	14
	Conv Stride	14
Latent Fuse Neck	Depth	12
	Num Latent Tokens	256/512/1024
	Hidden Dim	768
	Num Heads	16
	MLP Ratio	4
Latent Query Decoder	Depth	16
	Patch Size	14
	Hidden Dim	768
	Num Heads	16
	MLP Ratio	4
	DPT Layer Index	[3, 7, 11, 15]
(b) Hyperparameters		
Loss Weights	$\lambda_1, \lambda_2, \lambda_3$	1.0, 0.75, 1.0
Training Details	lr schedule	Cosine Decay
	lr	2e-4
	Warmup Steps	8000
	Optimizer	AdamW
	β_1, β_2	0.9, 0.95
	Gradient Clip	1.0
	Iterations	120000
	Disc Start Iter	50000
	Adv Loss Start Iter	60000
	Noise τ	0.8
	Pixel Count per Image	37000∼75500
	Aspect Ratio	0.7∼1.8
	Image per GPU	6∼18
	Mask Probability	0.1
	Mask Ratio	0.1∼0.6

Table 5: **Details of 3DRAE architecture and hyperparameters.**

A.1 Frozen 2D Encoder

For any given frozen 2D representation encoder, we use its pre-trained ViT-Base model and follow the protocols presented in RAE[1] if not otherwise specified. In particular, we discard any [CLS] or [REG] token produced by 2D encoder, and keep all of the patch tokens. Notably, since our 3D latent

representation is not directly derived from 2D encoder but processed and output by our Latent Fuse Neck, we do not have to ensure the tokens of 2D encoder to have zero mean and unit variance. Thus we just keep the original layer normalization in ViT architecture at the end of 2D encoder.

During training, we adopt dynamic image resolutions while ensuring that both height and width are divisible by 14. Since different 2D encoders employ varying patch sizes (e.g., 14 for DINOv2[48] and DA3[43], or 16 for SigLIP2[49]), we resize all input images to a common resolution divisible by 14 before feeding them into the 2D encoder. This ensures that the resulting token counts are consistent with those produced under a patch size of 14, enabling uniform processing across different encoder backbones. For example, for an image at resolution 336×296 that produces 336×296/14/14=504 tokens under a patch size of 14, we resize it to (336/14*16)×(296/14*16) resolution for SigLIP2 backbone, or keep the original 336×296 resolution for DINOv2 and DA3 backbones.

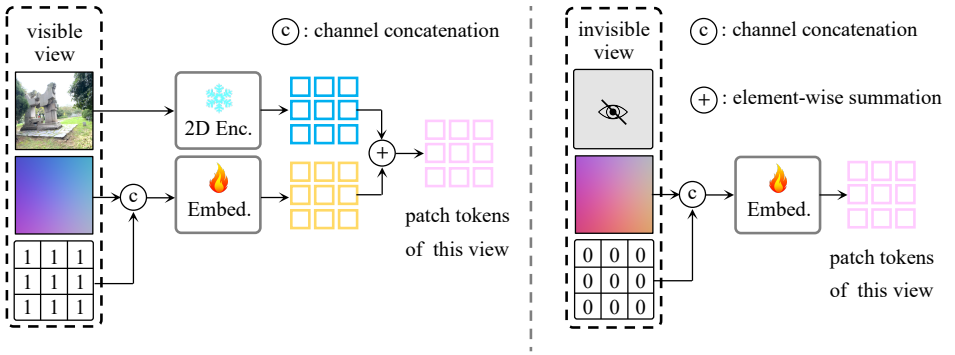
A.2 Latent Fuse Neck

Our Latent Fuse Neck consists of 12 transformer layers that process the concatenation of multi-view patch tokens and 3D latent tokens. Through global self attention[42], it enables thorough information exchange between these tokens, effectively fusing multi-view information into the 3D latent tokens. Following the practice in RAE[1], we apply layer normalization with no learned affine parameter at the end of Latent Fuse Neck to ensure each 3D latent token has zero mean and unit variance. After the layer normalization, we apply batch normalization with mean and variance globally computed on ImageNet dataset[73] to normalize the distribution of our 3D latent representation.

A.3 Latent Query Decoder

Our Latent Query Decoder consists of 16 transformer layers that process the concatenation of ray map tokens and multi-view fused 3D latent tokens. Through global self attention[42], target-view information in the multi-view fused 3D latent tokens can be queried and retrieved by the ray map tokens to predict target-view images. We extract ray map tokens for each target view from the output of the final transformer layer. These tokens, which encode necessary target view information, are then reshaped via unpatchification with a patch size of 14 to produce high-resolution images. For optional point map output, we adopt a separate Latent Query Decoder with DPT head[62] aggregating features from the 3rd, the 7th, the 11th and the 15th transformer layers for dense prediction. Since our 3D latent representation is decoupled from the input multi-view images, we can query it with ray maps of arbitrary views to render the corresponding images and point maps.

To enhance the decoder's generalization to the deviated latent space of diffusion model, we follow [1] to augment our 3D latent tokens with additive noise during training for robust decoding.



(a) Set mask to "1" for visible views (b) Set mask to "0" for invisible views

Figure 6: **Details of View Masking.**

A.4 Random Masking Strategy

To improve the robustness of our 3DRAE to missing views and enable compatibility with diverse conditioning configurations (i.e., varying numbers of visible views), we introduce a random masking strategy during training of 3DRAE. Specifically, we randomly mask out a set of multi-view images with probability 0.1, and for each masked sample, we randomly set 60% to 90% of the views as

invisible. As shown in Fig.6, visibility is indicated by binary masks: all-ones for visible views, all-zeros for invisible views. For a visible view, we concatenate an all-ones mask with its Plücker ray map and feed them into the ray map embedding module. The resulting ray map tokens—now encoding visibility—are summed with patch tokens from the frozen 2D encoder to produce the final patch tokens. For an invisible view, we concatenate an all-zeros mask with its ray map; the resulting ray map tokens encode only pose information and directly serve as the final patch tokens. With a 3DRAE trained under this masking strategy, we can encode camera poses from a complete trajectory alongside partially observed images. The resulting conditioning signals thus contain full spatial extent information, requiring the 3DDiT to generate only the spatially-consistent appearance of invisible views.

A.5 Impact of Adversarial Loss

We incorporate adversarial loss into our 3DRAE training. A discriminator, initialized from DINOv2-Small[48], is tasked with distinguishing between images produced by our decoder and real images, enforcing alignment between the predicted and ground-truth image distributions. Since such adversarial loss is commonly used in VAE training but has not been previously explored in novel view synthesis, we ablate its effect on rendering quality in Fig.7. Interestingly, we observe that incorporating the adversarial loss leads to noticeable improvements in image quality, particularly when the target view differs substantially from the input views in terms of pose. We posit that the adversarial loss enhances the robustness of image rendering to pose variations.

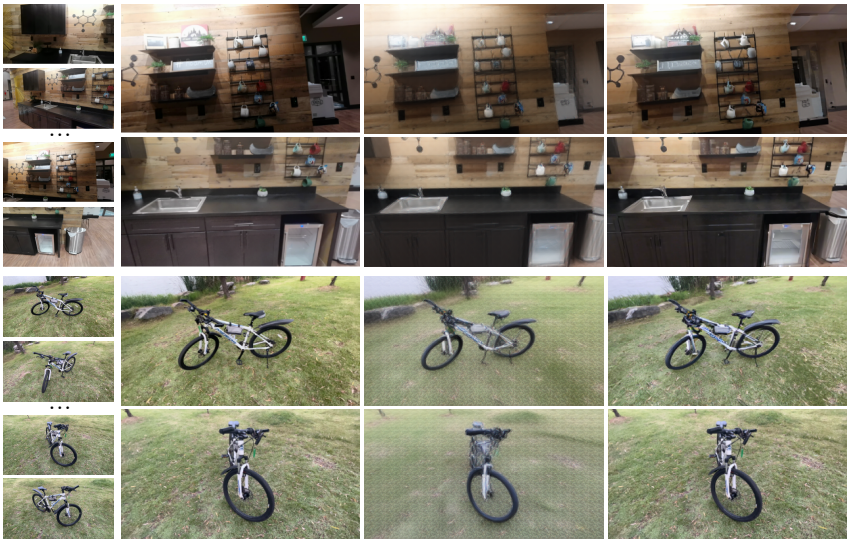


Figure 7: **Impact of Adversarial Loss.**

B 3DDiT Implementation

B.1 Diffusion Transformer Model

We use LightningDiT[64] as the backbone of our 3DDiT model by default. Following [1], we append a shallow but wide DDT head[59] to the LightningDiT backbone for high-dimensional 3D latent denoising. A continuous time schedule with time step restricted to real values in $[0, 1]$ is employed for flow matching formulation, where the time step embedding is obtained from a Gaussian Fourier embedding layer. We also adopt a dimension-dependent noise schedule shift[74] during training. For a schedule $t_n \in [0, 1]$ and 3D latent token count N with dimension M, the shifted timestep is calculated as $t_m = \frac{\alpha t_n}{1+(\alpha-1)t_n}$ where $\alpha = \sqrt{N \times M/D}$ is a dimention-dependent scaling factor. We follow [74] to set $D = 4096$ as the base dimension and $N \times M$ denotes the effective data dimension of our 3D latent space.

Detailed architecture and hyperparameter settings for 3DDiT at each model size are shown in Table 6. In general, our 3DDiT is firstly trained for 80k steps on ImageNet[73], and further trained for 80k

steps on the same collection of multi-view datasets as the training of 3DRAE. The difference is that, to enable our 3DDiT to support diverse multi-view conditioning configurations (i.e., unconditioning with number of views = 0, single-view conditioning with number of views = 1, sparse-view conditioning with number of views > 1), we set the masking probability to 1.0 to ensure we always use partial observed views as condition and set the masking ratio ranging from 0.6 to 0.9 to vary the number of observed views in condition. To enable complete unconditioning with no observed view, we randomly drop all views and only keep the poses at a probability 0.1. During the pre-training stage, such unconditioning is achieved by randomly drop class label conditions at a probability 0.1. The class label embedding layer is dropped after the pre-training stage.

(a) Network Architecture		
LightningDiT Backbone[64]	**3DDiT-S**	
	Depth	12
	Hidden Dim	384
	Num Heads	6
	3DDiT-B	
	Depth	12
	Hidden Dim	768
	Num Heads	12
	3DDiT-XL	
	Depth	28
	Hidden Dim	1152
	Num Heads	16
DDT Head[59]	Depth	2
	Hidden Dim (Width)	2048
	Num Heads	16
(b) Hyperparameters		
Training Details	lr schedule	Cosine Decay
	lr	2e-4
	Warmup Steps	8000
	Optimizer	AdamW
	β_1, β_2	0.9, 0.95
	Ema Decay	0.9995
	Gradient Clip	1.0
	Iterations	80000
	Condition Drop Probability	0.1
	Pixel Count per Image	37000$\sim$75500
	Aspect Ratio	0.7$\sim$1.8
	Image per GPU	6$\sim$18
	Mask Probability	1.0
	Mask Ratio	0.6$\sim$0.9

Table 6: **Details of 3DDiT architecture and hyperparameters.**

B.2 Sampling Details

During sampling of 3DDiT, we use standard ODE sampling with Euler sampler and 50 steps by default. We also use classifier-free guidance (CFG) during sampling to balance diversity and fidelity. Specifically, for unconditional prediction required by CFG, we directly drop the observed view images but keep the corresponding poses to ensure the conditioning latent tokens obtained from 3DRAE only contain the spatial extent information with no appearance constraint. For simplicity, we always set CFG scale to 2.0 during sampling for all conditioning configurations in our experiments.

C Training Datasets

We preprocess the raw datasets listed in Table 7 to train our 3DRAE and 3DDiT models. This collection covers a wide range of scenarios including indoor, outdoor, in-the-wild, object-centric and general scenes, enabling us to scale our method to large-scale data. To balance domain variance across datasets, we assign each dataset a sampling weight that determines its probability of being sampled during training, independent of the number of scenes and frames it contains. The preprocessing of

Name	Domain	#Scenes	#Frames	Weight
CO3D[71]	Indoor/Object	27K	2.6M	7.1%
WildRGBD[75]	Indoor/Object	19k	6.8M	5.1%
ARKitScenes[76]	Indoor/Scene	3.4K	0.9M	13.2%
ScanNet[72]	Indoor/Scene	1.2K	1.9M	6.3%
ScanNet++[77]	Indoor/Scene	855	0.7M	3.4%
Taskonomy[78]	Indoor/Scene	537	4.6M	4.2%
HM3D[79]	Indoor/Scene	899	9.5M	4.7%
Hypersim[80]	Indoor/Scene	767	74K	5.0%
RE10K[70]	Indoor/Scene	66k	8.9M	17.3%
Waymo[81]	Outdoor/Driving	798	0.8M	6.3%
Mapillary[82]	Outdoor/Driving	74	27K	0.6%
Virtual KITTI[83]	Outdoor/Driving	50	21K	0.7%
MVS-Synth[84]	Outdoor/Driving	120	12K	0.6%
DL3DV[69]	Outdoor/Scene	6k	2.2M	8.4%
BlendedMVG[85]	In-the-wild/Scene	501	115K	5.3%
MegaDepth[86]	In-the-wild/Scene	213	123K	0.6%
TartanAir[87]	In-the-wild/Scene	369	307K	3.9%
ImageNet[73]	In-the-wild/Scene	1.3M	1.3M	8.4%

Table 7: **Training Datasets.**

these datasets follows the protocol presented in the official implementation of CUT3R[45] if not otherwise specified. For RE10K[70] without ground-truth depth, we directly disable the point map supervision during training. For single-image data in ImageNet[73], which has no pose annotation, we leverage MoGe2[88] to estimate camera intrinsics for each image. Given a set of multi-view images, we align all camera poses to the coordinate frame of the first view, which serves as the world frame. The distance of the farthest camera from the first view is then used as a scale factor to normalize all poses, ensuring consistent scale across different datasets. For each data sample, all the images are cropped and resized to a random combination of resolution and aspect ratio with the pixel count constrained to a predefined range. The number of multi-view images per data sample is randomly selected from a predefined range. Based on the number of views and pixel count, we dynamically adjust the batch size to maintain a stable total number of tokens to be processed. Please see Table 5 and Table 6 for specific hyperparameter settings.

D Benchmark Details

To comprehensively evaluate the performance of our method, we construct a benchmark comprising 358 scenes from DL3DV[69], RE10K[70], CO3D[71] and ScanNet[72], covering diverse scene types including indoor, outdoor, object-level, and general scenarios. All the scenes are unseen during training, and are randomly selected subject to the constraint that the camera rotation and translation variation from the first to the last view exceeds an empirical threshold. This ensures substantial camera motion for thoroughly assessing the models' generative capabilities. For each scene, we uniformly downsample the original video or image sequence to 16 views, which serves as the minimum evaluation unit. To accommodate different conditioning configurations with varying numbers of observed views, we further sample from the 16 views accordingly. For single-view conditioning, we take only the first view as the observed view. For sparse-view conditioning, we uniformly sample observed views from the 16 views. All the 16 views excluding the observed ones are used for evaluation. In our evaluation, we employ multiple metrics. Photometric metrics including PSNR and LPIPS are used to measure reconstruction quality. Image distribution metric FID assesses generated image quality. To evaluate spatial consistency, we adopt pose accuracy metrics following prior work[28]. Specifically, ATE_r and ATE_t compute rotation and translation errors between poses of generated multi-view images and ground-truth poses, based on SLAM evaluation protocols[89, 90]. The poses of generated images are estimated using VGGT[42] with bundle adjustment[91].

E Video Comparison on Long-Trajectory Generation

Although our method primarily focuses on generating a queryable 3D latent representation of appearance and geometry across different poses, rather than producing videos composed of dense frame images, our 3DRAE decoder nevertheless support long-trajectory video rendering by querying our generated 3D latent representation at varying poses along a long trajectory.

In the supplementary video file `video_compare.mp4`, we present video results for long-trajectory (> 100 frames) generation alongside a comparison with baseline methods. As can be seen from the video, whereas 2D diffusion-based approaches struggle to render spatially consistent videos across different poses, our method accurately aligns with varying poses along a long trajectory. Taking SEVA [27] as an example, such approaches typically divide a long target trajectory into multiple chunks, generate each chunk separately, and then concatenate the results. This inevitably introduces spatial inconsistencies across chunks: the scene appearance generated in the current chunk changes in the next chunk, and the poses often exhibit abrupt jumps. Moreover, compared to 2D diffusion-based methods that only generate frame images, our method simultaneously obtains a point map for each pose, enabling the construction of a scene point cloud and thus achieving truly 3D-level scene generation. In comparison with regression-based methods, approaches such as LVSM [44] and DepthSplat [36] are unable to complete unseen scene appearance without generative modeling. Consequently, when the pose undergoes large changes, the rendered images exhibit drift or collapse. In contrast, our method can generate plausible appearance for unseen regions.

We also note that, for long-trajectory video generation, 2D diffusion-based methods require per-frame denoising, which is highly time-consuming. In contrast, our method generates the 3D latent tokens of the scene in a single pass. When rendering video frames, no heavy denoising is needed, where we simply query our 3DRAE decoder to predict the image for each target pose, incurring a computational cost comparable to that of regression-based approaches. Therefore, compared to the task that only generate a small number of novel-view images, our approach offers a significant efficiency advantage in long-trajectory video generation. Specifically, in Table 8, we report the average per-frame inference time when generating a 100-frame long-trajectory video, and find that our method is significantly faster than 2D diffusion-based methods (e.g., MotionCtrl [22], ViewCrafter [28], SEVA [27]) while being comparable to regression-based approaches (e.g., LVSM [44], DepthSplat [36]).

	MotionCtrl [22]	ViewCrafter [28]	SEVA [27]	DepthSplat [36]	LVSM [44]	Ours
sec./frame	0.738	12.638	5.325	0.010	0.013	0.032

Table 8: **Per-frame inference time comparison for 100-frame long-trajectory video generation.**

F Visual Results

In the supplementary video file `3D_gen.mp4`, we include additional 3D scene generation results under diverse conditioning configurations, as well as zero-shot results on unseen domains. The details are as follows.

F.1 Additional 3D Scene Generation Results

Single-View Conditioning. In Fig.8, we present extensive results of single-view conditioned 3D scene generation. For each sample, we provide 3DDiT with a single image as the conditional observation, along with a variable-length pose sequence specifying the spatial extent. As demonstrated, our method performs remarkably well on both object-level (rows 1∼2), outdoor scene-level (rows 3∼5) and indoor scene-level (rows 6∼8) 3D generation. It supports pose sequences of varying lengths and decodes images at different resolutions and aspect ratios, highlighting the advantage of our 3DRAE: the decoupling of 3D latent representation from multi-view observations.

Sparse-View Conditioning. In Fig.9, we present extensive results of sparse-view conditioned (i.e., number of views > 1) 3D scene generation. As shown in the figure, our method consistently generates plausible 3D scenes under varying numbers of conditional views (rows 1∼2 with 2 views and rows 3∼4 with 6 views). This demonstrates its highly competitive performance even in sparse-view settings where reconstruction fidelity is prioritized.

Unconditioning. In Fig.10, we further show the results of unconditional 3D scene generation where we only provide 3DDiT with only camera trajectory as input condition but no image observation. By varying the random seed, we can generate scenes with diverse appearances within the same spatial scope defined by a fixed camera trajectory. This demonstrates that our trained 3DDiT possesses the capability to synthesize general scene appearances even in the absence of image observations.

F.2 Zero-Shot Results

As shown in Fig.11, we further evaluate the zero-shot generalization capability of our approach on three datasets unseen during training: Tanks and Temples[92], Mip-NeRF 360[93], and DTU[94]. These span indoor, outdoor, and object-centric scenes, presenting diverse out-of-domain challenges. Despite not being trained on web-scale data like multi-view or video diffusion models, our method exhibits strong generalization performance across diverse domains, demonstrating its potential for real-world applications.

G 3DRAE under Extremely Dense Multi-View Observation

Although our 3DRAE was trained with at most 18 views per scene to learn compact 3D latent representations, we investigate its behavior under significantly denser observational views in Fig.12. To our surprise, our 3DRAE can represent extremely densely observed scenes with up to 128 views using only 1024 3D latent tokens, without degradation in reconstruction quality compared to the 16-view setting. This demonstrates the strong capability of our 3DRAE to generalize to large-scale scenes with many more observational views while maintaining fixed and compact representation complexity. Please refer to the supplementary video file `dense_recon.mp4` for better visualization.

H Broader Impacts

Our method introduces a novel paradigm: repurposing 2D representation models to derive 3D-grounded latent representation for 3D scenes. Such 3D latent representation preserves the rich semantics inherent in 2D models while being grounded with 3D awareness through supervision on novel view synthesis and point map reconstruction. Crucially, such compact 3D latent representation is substantially more efficient than representing 3D scenes as multi-view images or videos. By performing diffusion modeling directly within this 3D latent space at scale, we demonstrate efficient 3D scene generation with strong spatial consistency, validating the potential of this 3D latent representation as a powerful alternative to multi-view 2D latent representation commonly adopted in prior works[21, 22, 27–30].

More broadly, this 3D latent space, particularly when derived from SigLIP2, is naturally compatible with mainstream large multimodal models[95, 96]. Potentially, it enables the conversion of multi-view observed 3D scenes into a fixed length set of 3D-aware and language-aligned tokens, facilitating 3D scene understanding without relying on image- or video-based large multimodal models as in many existing approaches[97–100]. This opens new possibilities toward building embodied agents that unify 3D worlds and language. Furthermore, our 3D latent space holds promise for unifying 3D scene understanding and generation within shared representation, contributing to the development of physical world models. These promising directions are worth pursuing in future studies.

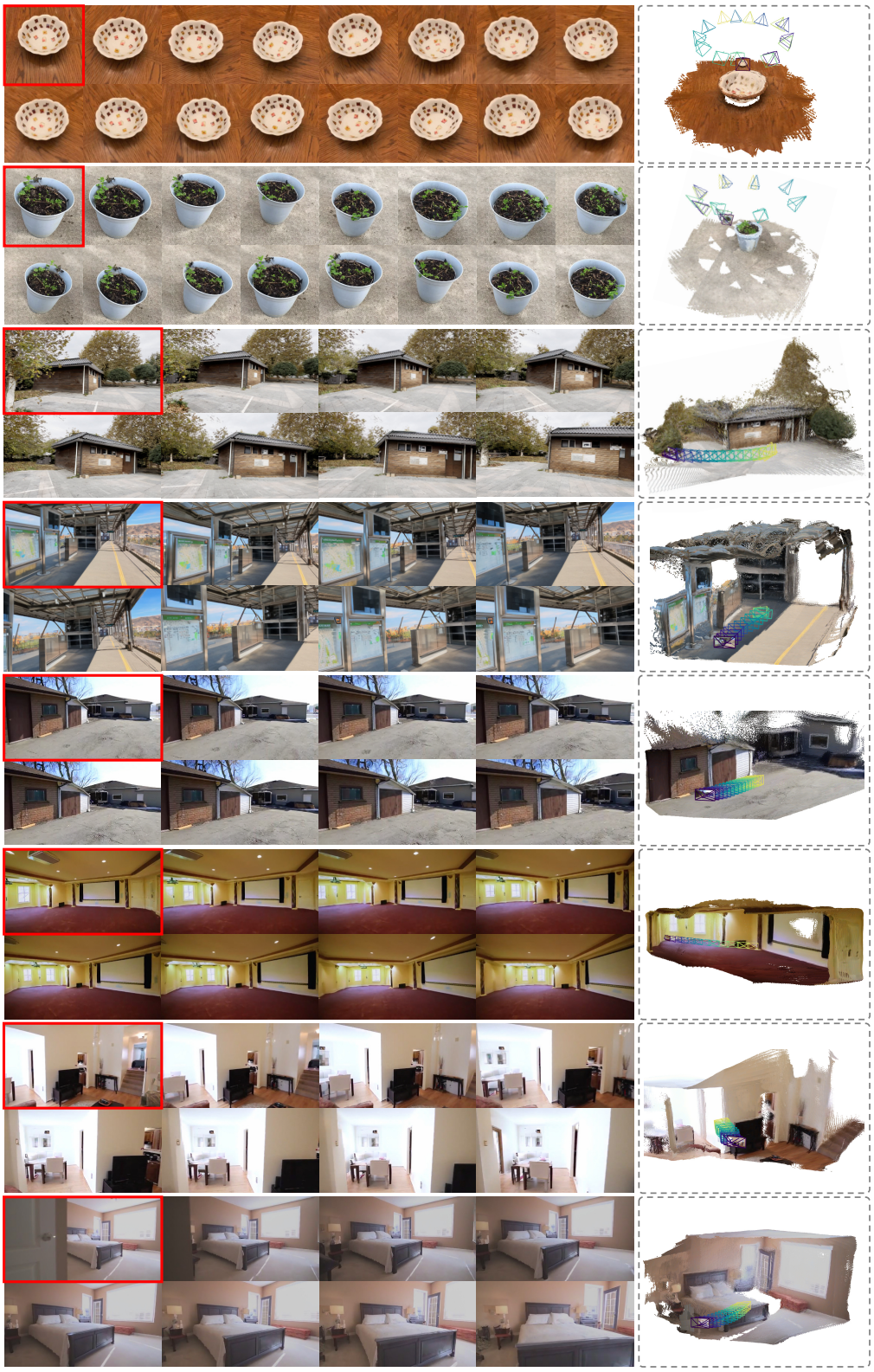


Figure 8: **Generated 3D Scenes under Single-View Conditioning.** The red bounding boxes denote the conditional views. Generated point clouds are shown on the right.



Figure 9: **Generated 3D Scenes under Sparse-View Conditioning.** The red bounding boxes denote the conditional views. Generated point clouds are shown on the right.

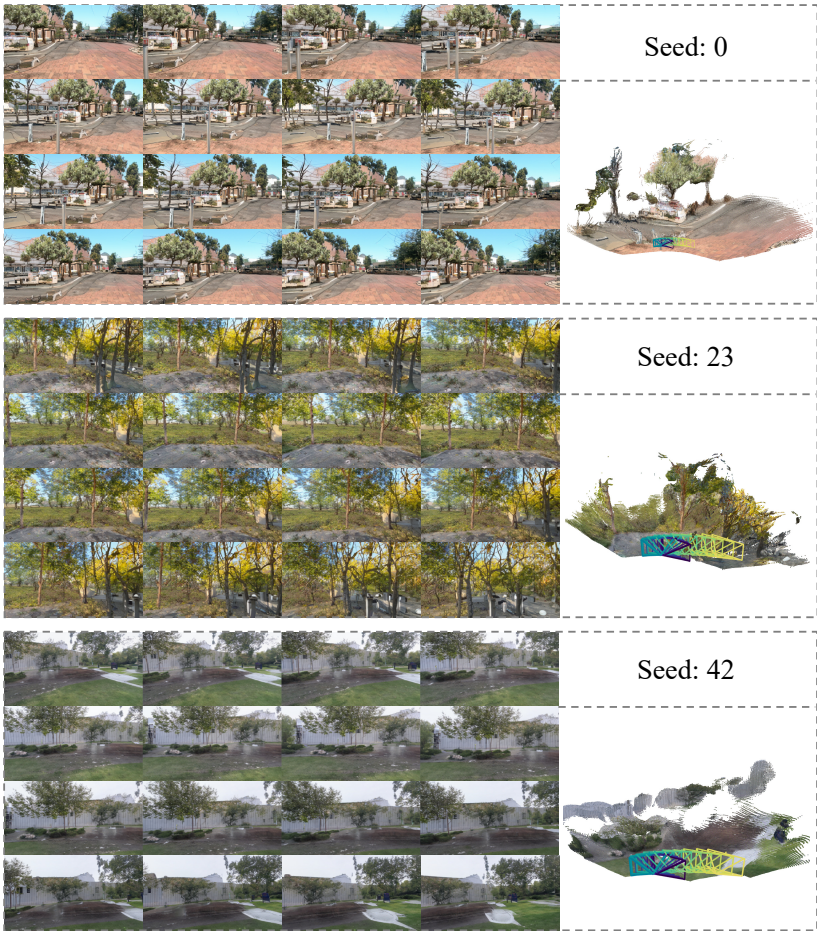


Figure 10: **Generated 3D Scenes without Appearance Conditioning.** Using the same camera trajectory condition with different random seeds, we generate 3D scenes with varied appearances.

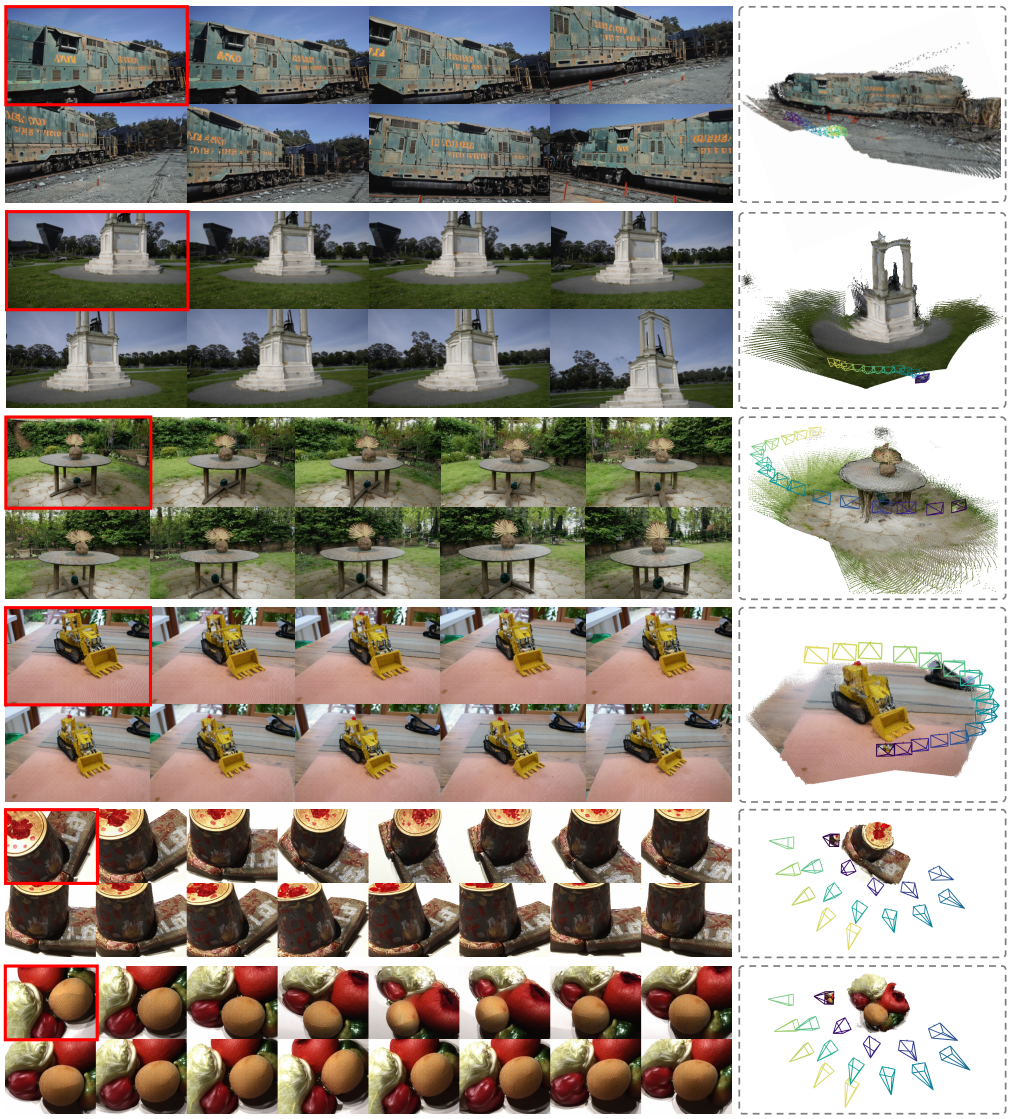


Figure 11: **Zero-Shot Generated 3D Scenes under Single-View Conditioning. Rows 1∼2:** results on Tanks and Temples dataset[92]. **Rows 3∼4:** results on Mip-NeRF 360 dataset[93]. **Rows 5∼6**: results on DTU dataset[94]. The red bounding boxes denote the conditional views. Generated point clouds are shown on the right.

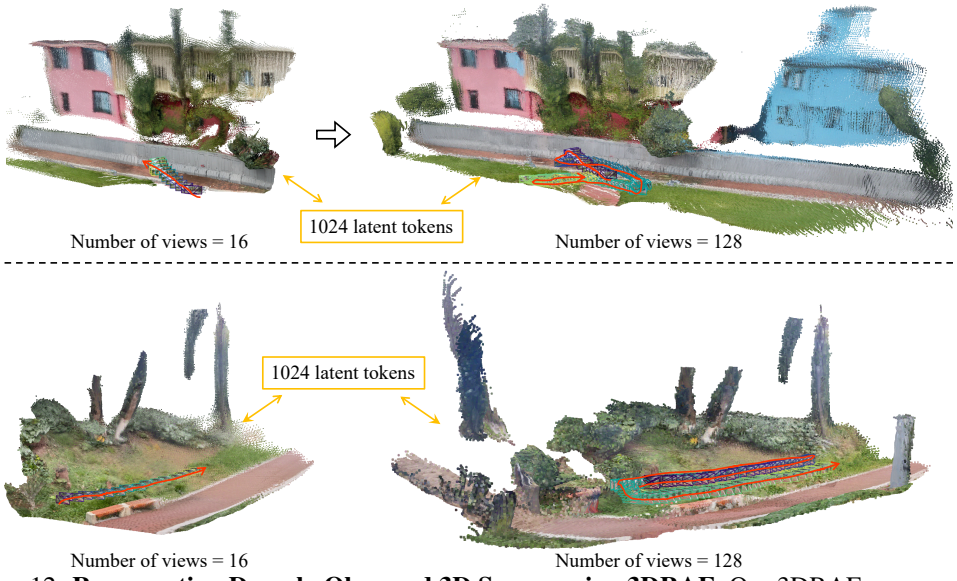


Figure 12: **Representing Densely Observed 3D Scenes using 3DRAE.** Our 3DRAE can represent the same 3D scenes but observed by different numbers of views (16 vs. 128 views) using the same set of 1K tokens. The red arrows highlight conditioning camera trajectories that specify the spatial extents of the generated scenes.

NeurIPS Paper Checklist

The checklist is designed to encourage best practices for responsible machine learning research, addressing issues of reproducibility, transparency, research ethics, and societal impact. Do not remove the checklist: **The papers not including the checklist will be desk rejected.** The checklist should follow the references and follow the (optional) supplemental material. The checklist does NOT count towards the page limit.

Please read the checklist guidelines carefully for information on how to answer these questions. For each question in the checklist:

- You should answer [Yes], [No], or [N/A].
- [N/A] means either that the question is Not Applicable for that particular paper or the relevant information is Not Available.
- Please provide a short (1–2 sentence) justification right after your answer (even for [N/A]).

The checklist answers are an integral part of your paper submission. They are visible to the reviewers, area chairs, senior area chairs, and ethics reviewers. You will also be asked to include it (after eventual revisions) with the final version of your paper, and its final version will be published with the paper.

The reviewers of your paper will be asked to use the checklist as one of the factors in their evaluation. While [Yes] is generally preferable to [No], it is perfectly acceptable to answer [No] provided a proper justification is given (e.g., error bars are not reported because it would be too computationally expensive" or "we were unable to find the license for the dataset we used"). In general, answering [No] or [N/A] is not grounds for rejection. While the questions are phrased in a binary way, we acknowledge that the true answer is often more nuanced, so please just use your best judgment and write a justification to elaborate. All supporting evidence can appear either in the main paper or the supplemental material, provided in appendix. If you answer [Yes] to a question, in the justification please point to the section(s) where related material for the question can be found.

IMPORTANT, please:

- **Delete this instruction block, but keep the section heading "NeurIPS Paper Checklist"**,
- **Keep the checklist subsection headings, questions/answers and guidelines below.**
- **Do not modify the questions and only use the provided macros for your answers**.

1. **Claims**

   Question: Do the main claims made in the abstract and introduction accurately reflect the paper's contributions and scope?

   Answer: [Yes]

   Justification: We have clearly stated the contributions and scope in the Abstract and Introuction.

   Guidelines:

   - The answer [N/A] means that the abstract and introduction do not include the claims made in the paper.
   - The abstract and/or introduction should clearly state the claims made, including the contributions made in the paper and important assumptions and limitations. A [No] or [N/A] answer to this question will not be perceived well by the reviewers.
   - The claims made should match theoretical and experimental results, and reflect how much the results can be expected to generalize to other settings.
   - It is fine to include aspirational goals as motivation as long as it is clear that these goals are not attained by the paper.

2. **Limitations**

   Question: Does the paper discuss the limitations of the work performed by the authors?

   Answer: [Yes]

Justification: We have discussed the limitations in Sec. 5 of our Appendix.

Guidelines:

- The answer [N/A] means that the paper has no limitation while the answer [No] means that the paper has limitations, but those are not discussed in the paper.
- The authors are encouraged to create a separate "Limitations" section in their paper.
- The paper should point out any strong assumptions and how robust the results are to violations of these assumptions (e.g., independence assumptions, noiseless settings, model well-specification, asymptotic approximations only holding locally). The authors should reflect on how these assumptions might be violated in practice and what the implications would be.
- The authors should reflect on the scope of the claims made, e.g., if the approach was only tested on a few datasets or with a few runs. In general, empirical results often depend on implicit assumptions, which should be articulated.
- The authors should reflect on the factors that influence the performance of the approach. For example, a facial recognition algorithm may perform poorly when image resolution is low or images are taken in low lighting. Or a speech-to-text system might not be used reliably to provide closed captions for online lectures because it fails to handle technical jargon.
- The authors should discuss the computational efficiency of the proposed algorithms and how they scale with dataset size.
- If applicable, the authors should discuss possible limitations of their approach to address problems of privacy and fairness.
- While the authors might fear that complete honesty about limitations might be used by reviewers as grounds for rejection, a worse outcome might be that reviewers discover limitations that aren't acknowledged in the paper. The authors should use their best judgment and recognize that individual actions in favor of transparency play an important role in developing norms that preserve the integrity of the community. Reviewers will be specifically instructed to not penalize honesty concerning limitations.

3. **Theory assumptions and proofs**

   Question: For each theoretical result, does the paper provide the full set of assumptions and a complete (and correct) proof?

   Answer: [Yes]

   Justification: We established our assumptions and proofs upon papers cited.

   Guidelines:

   - The answer [N/A] means that the paper does not include theoretical results.
   - All the theorems, formulas, and proofs in the paper should be numbered and cross-referenced.
   - All assumptions should be clearly stated or referenced in the statement of any theorems.
   - The proofs can either appear in the main paper or the supplemental material, but if they appear in the supplemental material, the authors are encouraged to provide a short proof sketch to provide intuition.
   - Inversely, any informal proof provided in the core of the paper should be complemented by formal proofs provided in appendix or supplemental material.
   - Theorems and Lemmas that the proof relies upon should be properly referenced.

4. **Experimental result reproducibility**

   Question: Does the paper fully disclose all the information needed to reproduce the main experimental results of the paper to the extent that it affects the main claims and/or conclusions of the paper (regardless of whether the code and data are provided or not)?

   Answer: [Yes]

   Justification: All relevant details are provided within the text of our main paper and appendix, or through the references we have cited.

   Guidelines:

- The answer [N/A] means that the paper does not include experiments.
- If the paper includes experiments, a [No] answer to this question will not be perceived well by the reviewers: Making the paper reproducible is important, regardless of whether the code and data are provided or not.
- If the contribution is a dataset and/or model, the authors should describe the steps taken to make their results reproducible or verifiable.
- Depending on the contribution, reproducibility can be accomplished in various ways. For example, if the contribution is a novel architecture, describing the architecture fully might suffice, or if the contribution is a specific model and empirical evaluation, it may be necessary to either make it possible for others to replicate the model with the same dataset, or provide access to the model. In general. releasing code and data is often one good way to accomplish this, but reproducibility can also be provided via detailed instructions for how to replicate the results, access to a hosted model (e.g., in the case of a large language model), releasing of a model checkpoint, or other means that are appropriate to the research performed.
- While NeurIPS does not require releasing code, the conference does require all submissions to provide some reasonable avenue for reproducibility, which may depend on the nature of the contribution. For example
  (a) If the contribution is primarily a new algorithm, the paper should make it clear how to reproduce that algorithm.
  (b) If the contribution is primarily a new model architecture, the paper should describe the architecture clearly and fully.
  (c) If the contribution is a new model (e.g., a large language model), then there should either be a way to access this model for reproducing the results or a way to reproduce the model (e.g., with an open-source dataset or instructions for how to construct the dataset).
  (d) We recognize that reproducibility may be tricky in some cases, in which case authors are welcome to describe the particular way they provide for reproducibility. In the case of closed-source models, it may be that access to the model is limited in some way (e.g., to registered users), but it should be possible for other researchers to have some path to reproducing or verifying the results.

5. **Open access to data and code**

   Question: Does the paper provide open access to the data and code, with sufficient instructions to faithfully reproduce the main experimental results, as described in supplemental material?

   Answer: [No]

   Justification: We promise we will release all the data and code upon the acceptance of our paper.

   Guidelines:

   - The answer [N/A] means that paper does not include experiments requiring code.
   - Please see the NeurIPS code and data submission guidelines (`https://neurips.cc/public/guides/CodeSubmissionPolicy`) for more details.
   - While we encourage the release of code and data, we understand that this might not be possible, so [No] is an acceptable answer. Papers cannot be rejected simply for not including code, unless this is central to the contribution (e.g., for a new open-source benchmark).
   - The instructions should contain the exact command and environment needed to run to reproduce the results. See the NeurIPS code and data submission guidelines (`https://neurips.cc/public/guides/CodeSubmissionPolicy`) for more details.
   - The authors should provide instructions on data access and preparation, including how to access the raw data, preprocessed data, intermediate data, and generated data, etc.
   - The authors should provide scripts to reproduce all experimental results for the new proposed method and baselines. If only a subset of experiments are reproducible, they should state which ones are omitted from the script and why.

- At submission time, to preserve anonymity, the authors should release anonymized versions (if applicable).
- Providing as much information as possible in supplemental material (appended to the paper) is recommended, but including URLs to data and code is permitted.

6. **Experimental setting/details**

   Question: Does the paper specify all the training and test details (e.g., data splits, hyperparameters, how they were chosen, type of optimizer) necessary to understand the results?

   Answer: [Yes]

   Justification: All relevant details are provided within the text of our main paper and appendix, or through the references we have cited.

   Guidelines:

   - The answer [N/A] means that the paper does not include experiments.
   - The experimental setting should be presented in the core of the paper to a level of detail that is necessary to appreciate the results and make sense of them.
   - The full details can be provided either with the code, in appendix, or as supplemental material.

7. **Experiment statistical significance**

   Question: Does the paper report error bars suitably and correctly defined or other appropriate information about the statistical significance of the experiments?

   Answer: [No]

   Justification: No, due to the high computational cost of training large diffusion models on massive multi-view datasets, we only performed one final training run and evaluated on fixed test sets. However, all the quantitative results we reported in our experiments were averaged over three runs with different random seeds for the test-time sampling process.

   Guidelines:

   - The answer [N/A] means that the paper does not include experiments.
   - The authors should answer [Yes] if the results are accompanied by error bars, confidence intervals, or statistical significance tests, at least for the experiments that support the main claims of the paper.
   - The factors of variability that the error bars are capturing should be clearly stated (for example, train/test split, initialization, random drawing of some parameter, or overall run with given experimental conditions).
   - The method for calculating the error bars should be explained (closed form formula, call to a library function, bootstrap, etc.)
   - The assumptions made should be given (e.g., Normally distributed errors).
   - It should be clear whether the error bar is the standard deviation or the standard error of the mean.
   - It is OK to report 1-sigma error bars, but one should state it. The authors should preferably report a 2-sigma error bar than state that they have a 96% CI, if the hypothesis of Normality of errors is not verified.
   - For asymmetric distributions, the authors should be careful not to show in tables or figures symmetric error bars that would yield results that are out of range (e.g., negative error rates).
   - If error bars are reported in tables or plots, the authors should explain in the text how they were calculated and reference the corresponding figures or tables in the text.

8. **Experiments compute resources**

   Question: For each experiment, does the paper provide sufficient information on the computer resources (type of compute workers, memory, time of execution) needed to reproduce the experiments?

   Answer: [Yes]

   Justification: We have reported the computer resources we used in the experiments section.

Guidelines:

- The answer [N/A] means that the paper does not include experiments.
- The paper should indicate the type of compute workers CPU or GPU, internal cluster, or cloud provider, including relevant memory and storage.
- The paper should provide the amount of compute required for each of the individual experimental runs as well as estimate the total compute.
- The paper should disclose whether the full research project required more compute than the experiments reported in the paper (e.g., preliminary or failed experiments that didn't make it into the paper).

9. **Code of ethics**

   Question: Does the research conducted in the paper conform, in every respect, with the NeurIPS Code of Ethics `https://neurips.cc/public/EthicsGuidelines`?

   Answer: [Yes]

   Justification: The research conducted in the paper conform the NeurIPS Code of Ethics.

   Guidelines:

   - The answer [N/A] means that the authors have not reviewed the NeurIPS Code of Ethics.
   - If the authors answer [No], they should explain the special circumstances that require a deviation from the Code of Ethics.
   - The authors should make sure to preserve anonymity (e.g., if there is a special consideration due to laws or regulations in their jurisdiction).

10. **Broader impacts**

    Question: Does the paper discuss both potential positive societal impacts and negative societal impacts of the work performed?

    Answer: [Yes]

    Justification: We have discussed the potential impacts of our paper in Sec. H of our Appendix.

    Guidelines:

    - The answer [N/A] means that there is no societal impact of the work performed.
    - If the authors answer [N/A] or [No], they should explain why their work has no societal impact or why the paper does not address societal impact.
    - Examples of negative societal impacts include potential malicious or unintended uses (e.g., disinformation, generating fake profiles, surveillance), fairness considerations (e.g., deployment of technologies that could make decisions that unfairly impact specific groups), privacy considerations, and security considerations.
    - The conference expects that many papers will be foundational research and not tied to particular applications, let alone deployments. However, if there is a direct path to any negative applications, the authors should point it out. For example, it is legitimate to point out that an improvement in the quality of generative models could be used to generate Deepfakes for disinformation. On the other hand, it is not needed to point out that a generic algorithm for optimizing neural networks could enable people to train models that generate Deepfakes faster.
    - The authors should consider possible harms that could arise when the technology is being used as intended and functioning correctly, harms that could arise when the technology is being used as intended but gives incorrect results, and harms following from (intentional or unintentional) misuse of the technology.
    - If there are negative societal impacts, the authors could also discuss possible mitigation strategies (e.g., gated release of models, providing defenses in addition to attacks, mechanisms for monitoring misuse, mechanisms to monitor how a system learns from feedback over time, improving the efficiency and accessibility of ML).

11. **Safeguards**

Question: Does the paper describe safeguards that have been put in place for responsible release of data or models that have a high risk for misuse (e.g., pre-trained language models, image generators, or scraped datasets)?

Answer: [N/A]

Justification: The released model does not have a high risk for misuse.

Guidelines:

- The answer [N/A] means that the paper poses no such risks.
- Released models that have a high risk for misuse or dual-use should be released with necessary safeguards to allow for controlled use of the model, for example by requiring that users adhere to usage guidelines or restrictions to access the model or implementing safety filters.
- Datasets that have been scraped from the Internet could pose safety risks. The authors should describe how they avoided releasing unsafe images.
- We recognize that providing effective safeguards is challenging, and many papers do not require this, but we encourage authors to take this into account and make a best faith effort.

12. **Licenses for existing assets**

Question: Are the creators or original owners of assets (e.g., code, data, models), used in the paper, properly credited and are the license and terms of use explicitly mentioned and properly respected?

Answer: [Yes]

Justification: We have cited the open-source code and datasets mentioned in the paper and adhered to the terms of use.

Guidelines:

- The answer [N/A] means that the paper does not use existing assets.
- The authors should cite the original paper that produced the code package or dataset.
- The authors should state which version of the asset is used and, if possible, include a URL.
- The name of the license (e.g., CC-BY 4.0) should be included for each asset.
- For scraped data from a particular source (e.g., website), the copyright and terms of service of that source should be provided.
- If assets are released, the license, copyright information, and terms of use in the package should be provided. For popular datasets, `paperswithcode.com/datasets` has curated licenses for some datasets. Their licensing guide can help determine the license of a dataset.
- For existing datasets that are re-packaged, both the original license and the license of the derived asset (if it has changed) should be provided.
- If this information is not available online, the authors are encouraged to reach out to the asset's creators.

13. **New assets**

Question: Are new assets introduced in the paper well documented and is the documentation provided alongside the assets?

Answer: [Yes]

Justification: We are committed to releasing our dataset and code as soon as possible.

Guidelines:

- The answer [N/A] means that the paper does not release new assets.
- Researchers should communicate the details of the dataset/code/model as part of their submissions via structured templates. This includes details about training, license, limitations, etc.
- The paper should discuss whether and how consent was obtained from people whose asset is used.

- At submission time, remember to anonymize your assets (if applicable). You can either create an anonymized URL or include an anonymized zip file.

14. **Crowdsourcing and research with human subjects**

    Question: For crowdsourcing experiments and research with human subjects, does the paper include the full text of instructions given to participants and screenshots, if applicable, as well as details about compensation (if any)?

    Answer: [N/A]

    Justification: This work does not involve crowdsourcing nor research with human subjects.

    Guidelines:

    - The answer [N/A] means that the paper does not involve crowdsourcing nor research with human subjects.
    - Including this information in the supplemental material is fine, but if the main contribution of the paper involves human subjects, then as much detail as possible should be included in the main paper.
    - According to the NeurIPS Code of Ethics, workers involved in data collection, curation, or other labor should be paid at least the minimum wage in the country of the data collector.

15. **Institutional review board (IRB) approvals or equivalent for research with human subjects**

    Question: Does the paper describe potential risks incurred by study participants, whether such risks were disclosed to the subjects, and whether Institutional Review Board (IRB) approvals (or an equivalent approval/review based on the requirements of your country or institution) were obtained?

    Answer: [N/A]

    Justification: This work does not involve crowdsourcing nor research with human subjects.

    Guidelines:

    - The answer [N/A] means that the paper does not involve crowdsourcing nor research with human subjects.
    - Depending on the country in which research is conducted, IRB approval (or equivalent) may be required for any human subjects research. If you obtained IRB approval, you should clearly state this in the paper.
    - We recognize that the procedures for this may vary significantly between institutions and locations, and we expect authors to adhere to the NeurIPS Code of Ethics and the guidelines for their institution.
    - For initial submissions, do not include any information that would break anonymity (if applicable), such as the institution conducting the review.

16. **Declaration of LLM usage**

    Question: Does the paper describe the usage of LLMs if it is an important, original, or non-standard component of the core methods in this research? Note that if the LLM is used only for writing, editing, or formatting purposes and does *not* impact the core methodology, scientific rigor, or originality of the research, declaration is not required.

    Answer: [N/A]

    Justification: Method development in this research does not involve LLMs as any important, original, or non-standard components.

    Guidelines:

    - The answer [N/A] means that the core method development in this research does not involve LLMs as any important, original, or non-standard components.
    - Please refer to our LLM policy in the NeurIPS handbook for what should or should not be described.